ACS central science

http://pubs.acs.org/journal/acscii

Research Article

A Single Immunization with Spike-Functionalized Ferritin Vaccines Elicits Neutralizing Antibody Responses against SARS-CoV-2 in Mice

Abigail E. Powell, Kaiming Zhang, Mrinmoy Sanyal, Shaogeng Tang, Payton A. Weidenbacher, Shanshan Li, Tho D. Pham, John E. Pak, Wah Chiu, and Peter S. Kim*

Cite This: ACS Cent. Sci. 2021, 7, 183−199

Read Online

ACCESS | Metrics & More | Article Recommendations | Supporting Information

ABSTRACT: The development of a safe and effective SARS-CoV-2 vaccine is a public health priority. We designed subunit vaccine candidates using self-assembling ferritin nanoparticles displaying one of two multimerized SARS-CoV-2 spikes: full-length ectodomain (S-Fer) or a C-terminal 70 amino-acid deletion (SΔC-Fer). Ferritin is an attractive nanoparticle platform for production of vaccines, and ferritin-based vaccines have been investigated in humans in two separate clinical trials. We confirmed proper folding and antigenicity of spike on the surface of ferritin by cryo-EM and binding to conformation-specific monoclonal antibodies. After a single immunization of mice with either of the two spike ferritin particles, a lentiviral SARS-CoV-2 pseudovirus assay revealed mean neutralizing antibody titers at least 2-fold greater than those in convalescent plasma from COVID-19 patients. Additionally, a single dose of SΔC-Fer elicited significantly higher neutralizing responses as compared to immunization with the spike receptor binding domain (RBD) monomer or spike ectodomain trimer alone. After a second dose, mice immunized with SΔC-Fer exhibited higher neutralizing titers than all other groups. Taken together, these results demonstrate that multivalent presentation of SARS-CoV-2 spike on ferritin can notably enhance elicitation of neutralizing antibodies, thus constituting a viable strategy for single-dose vaccination against COVID-19.

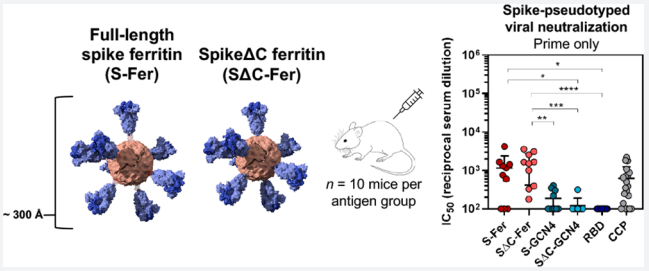

INTRODUCTION

The emergence of SARS-CoV-2 in the human population in 2019 has caused a rapidly growing pandemic that has disrupted nearly all global infrastructures. To date, there have been over 63 million confirmed cases of COVID-19 and nearly 1.5 million deaths worldwide.[1] While some nations have controlled viral spread through social distancing, widespread testing, and contact tracing, many nations struggle to contain the growing number of cases and are still experiencing extensive community spread. Additionally, the introduction of SARS-CoV-2 into low-resource settings will lead to severe and lasting impacts on economic and healthcare systems. Long-term control of the pandemic will require one or more effective vaccines that can be made widely available across the globe.

The primary viral target for protective antibody-based vaccines against COVID-19 is the SARS-CoV-2 spike, a trimeric surface glycoprotein responsible for viral entry.[2,3] Importantly, COVID-19 patients have been shown to elicit robust neutralizing antibody responses directed at the SARS-CoV-2 spike, which suggests that this antigen could be promising in the context of a protective vaccine.[4,5] The spike protein is produced as a single polypeptide and cleaved to form the S1 and S2 subunits, which are responsible for receptor binding (S1) and fusion with the host cell membrane (S2).[3,6,7] The receptor binding domain (RBD) is a 25 kDa domain of S1 that recognizes the SARS-CoV-2 human receptor, angiotensin converting enzyme 2 (ACE2), and can form a functionally folded domain when expressed separately from the rest of S1.[8−10]

A vast array of vaccination platforms are being employed for the development of a safe and effective SARS-CoV-2 vaccine.[11−19] Several vaccine candidates are currently being investigated in Phase 3 clinical trials including two mRNA-based vaccines and two virally vectored vaccines.[20−22] Importantly, the mRNA vaccine candidates rely on lipid−nanoparticle encapsulation and require long-term cold-chain storage (−20 to −80 °C),[20,21] leading to extensive logistical challenges for distribution and administration. Virus-based vaccines including inactivated, live-attenuated, and recombinant viral vaccines can produce robust immune responses, but are known to induce off-target vector-directed immune responses[23,24] and can be associated with more frequent side effects and adverse events.[25,26]

Received: October 16, 2020
Published: January 5, 2021

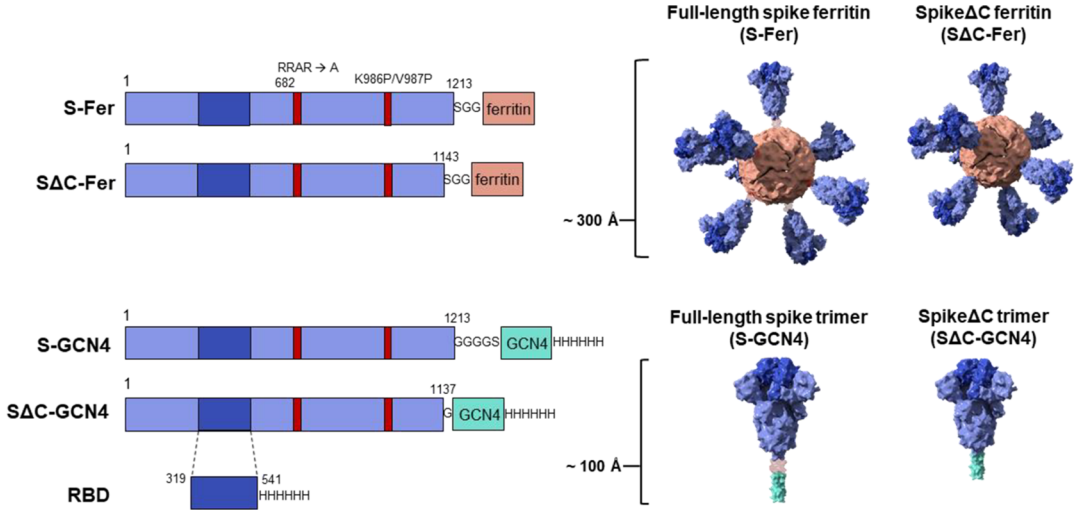

Figure 1. Construct design for SARS-CoV-2 spike-functionalized ferritin nanoparticles. All constructs are based on the Wuhan-Hu-1 amino acid sequence (GenBank MN9089473) of SARS-CoV-2 spike. Spike-functionalized ferritin constructs were made by fusing spike ectodomain (residues 1−1213) or spikeΔC (residues 1−1143) to the *H. pylori* ferritin subunit separated by an SGG linker. A structural representation based on the spike trimer cryo-EM structure (PDB 6VXX) and the *H. pylori* ferritin crystal structure (PDB 3BVE) depicts the 24-subunit particle displaying spike or spikeΔC on the surface. The estimated size of the spike-functionalized ferritin particles based on structural data is ∼300 Å. The S-GCN4 and SΔC-GCN4 trimer constructs were made by fusing either the full-length spike residues (1−1213) or spikeΔC (1−1137) to a modified GCN4 trimerization domain followed by a hexahistidine tag. A structural representation of the spike trimers based on the cryo-EM structure (PDB 6VXX) is shown with an estimate length of ∼100 Å. The RBD spans residues 319−541 of the spike protein and is preceded by the native signal peptide (not shown) and followed by a hexahistidine tag.

Subunit vaccines, in which a protein antigen from the pathogen is used to elicit a protective antibody response, are an attractive option for an accessible SARS-CoV-2 vaccine for reasons including safety, manufacturing scalability, and ease of distribution to low- and middle-income nations.[26] Though typically less immunogenic than virus-based vaccines, the immunogenicity of subunit vaccinations can be significantly increased by formulation with adjuvants.[25] It has also been demonstrated that multivalent presentation of antigens markedly enhances the immune response,[27,28] and several nanoparticle-based platforms have been utilized to multimerize antigens of interest to improve the antibody response to subunit vaccine candidates.[27−30] Furthermore, two recent studies have shown that the multivalent presentation of the SARS-CoV-2 RBD[31] as well as the spike ectodomain[32] using various multimerization platforms elicits better neutralizing antibody responses than nonmultimerized forms of the same antigens.

One such multimerization platform, *Helicobacter pylori* ferritin, has been used to display antigens from influenza,[33,34] HIV-1,[35,36] and Epstein−Barr virus,[30] among others.[37,38] *H. pylori* ferritin self-assembles into 24-subunit particles with eight 3-fold axes of symmetry.[39] Fusion of a single protomer of a viral glycoprotein to the N-terminal region of an *H. pylori* ferritin subunit facilitates assembly of a protein nanoparticle that displays eight copies of a trimeric antigen on the surface at the 3-fold axes.[33,39] Display of antigens on ferritin generally elicits a more robust neutralizing antibody response against the target pathogen as compared to immunization with the antigen alone.[30,33,35] Importantly, two influenza-functionalized ferritin vaccines have been shown to be safe and immunogenic in clinical trials (NCT03186781 and NCT03814720),[33,34] and robust pipelines have been established for large-scale manufacturing of ferritin-based vaccines.[40]

Here, we fused the full-length spike ectodomain (residues 1−1213) to *H. pylori* ferritin (denoted S-Fer; Figure 1) to determine the effect of antigen multimerization on elicitation of antibodies against SARS-CoV-2. Additionally, we designed a second nanoparticle construct in which we deleted the C-terminal 70 residues of the ectodomain and expressed this truncated spike (residues 1−1143) on ferritin (SΔC-Fer). These C-terminal residues are unresolved in the cryo-EM structures of the spike trimer,[3,7] and it has been suggested that they have extensive conformational flexibility based on electron microscopy of soluble trimers and viral particles.[41−43] Additionally, this region of the spike contains an immunodominant linear epitope, as determined via analysis of convalescent sera from COVID-19 patients.[44,45] We therefore hypothesized that deleting these residues would more readily facilitate formation of spike ferritin particles and could influence immunogenicity. As points of comparison, we also expressed and purified three additional antigens: spike trimer containing a GCN4-based trimerization domain either in full-length or SΔC form (denoted S-GCN4 and SΔC-GCN4)[46] and monomeric receptor binding domain (RBD) (Figure 1).

After expressing and purifying the S-Fer and SΔC-Fer nanoparticles, we confirmed that they were stable, homogeneous, and properly folded using biophysical, structural, and binding analyses including size-exclusion chromatography multiangle light scattering (SEC-MALS), cryoelectron microscopy (cryo-EM), and biolayer interferometry (BLI). To assess the immune response *in vivo*, we immunized mice and characterized the antibody responses to the spike ferritin particles versus S-GCN4, SΔC-GCN4, and RBD. After a single dose, mice immunized with SΔC-Fer exhibited a significantly higher neutralizing antibody response than all nonferritin groups as determined using a spike-pseudotyped lentiviral assay.[47,48] Importantly, immunization with a single dose of S-Fer or SΔC-Fer elicited at least 2-fold higher neutralizing titers

https://dx.doi.org/10.1021/acscentsci.0c01405
ACS Cent. Sci. 2021, 7, 183−199

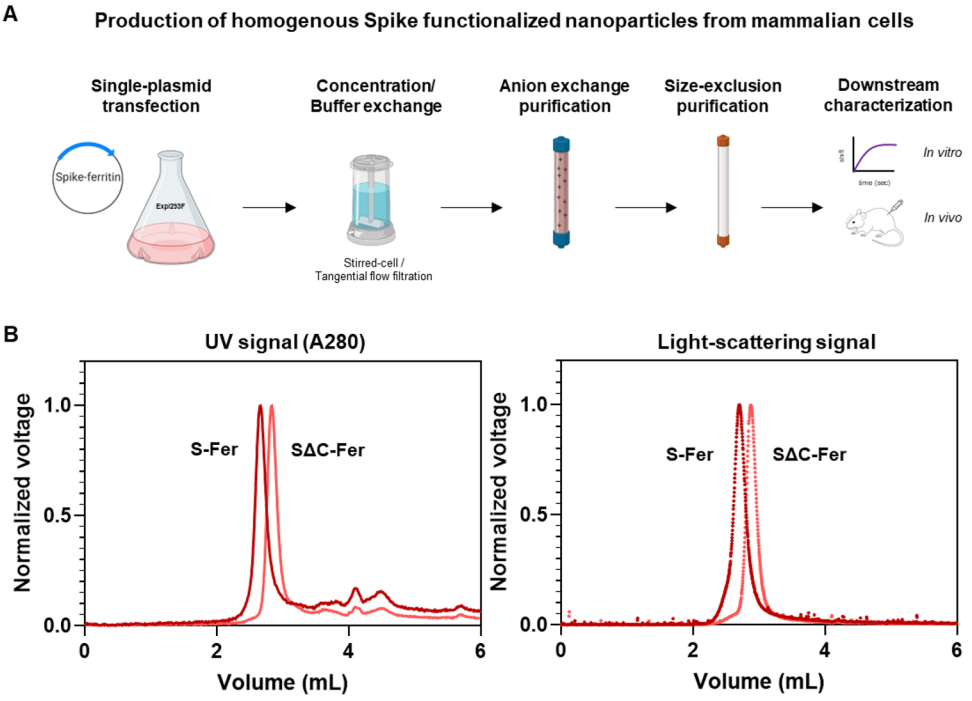

Figure 2. Spike ferritin nanoparticles can be expressed in mammalian cell culture and purified to homogeneity. (A) Scheme for expressing and purifying spike ferritin nanoparticle antigens in mammalian cells. Spike ferritin particle subunits are encoded in a single plasmid that is transfected into the Expi293F suspension human cell line. Expi293F cells are harvested, and culture supernatant is buffer exchanged and purified via anion exchange chromatography. Protein-containing fractions are identified via Western blot, pooled, and purified by size-exclusion chromatography (SRT SEC-1000). Purified nanoparticles are assessed using biophysical characterization methods including SDS-PAGE, analytical size-exclusion chromatography, and BLI follow by *in vivo* characterization of the immune responses elicited in mice. (B) SEC-MALS UV A280 (left) and light scattering signals (right) from analysis of spike-based ferritin antigens using an SRT SEC-1000 size-exclusion column. A single prominent peak in both the UV and light-scattering traces confirms that spike ferritin nanoparticle preparations are homogeneous and do not aggregate.

as those observed in plasma from convalescent COVID-19 patients. Taken together, these results provide insights into the development of SARS-CoV-2 subunit vaccines and demonstrate that spike-functionalized ferritin nanoparticles elicit an enhanced antibody response compared to the spike trimers or RBD alone.

RESULTS

Design of Spike-Functionalized Ferritin Nanoparticles. To design functionalized nanoparticles displaying the spike protein, we generated a fusion protein containing the spike ectodomain followed by *H. pylori* ferritin, a 19 kDa protein that self-assembles into a 24-subunit protein-based nanoparticle (Figure 1). Given the 3-fold symmetrical axes on the ferritin particle, fusion of a protomer to the N-terminus of this domain creates a functionalized particle that displays eight trimers on the surface.

We designed two versions of the spike-functionalized nanoparticle: one containing the full-length ectodomain (residues 1−1213; S-Fer) and one in which the C-terminus of the ectodomain was truncated (residues 1−1143; SΔC-Fer) (Figure 1). We sought to investigate whether deletion of this region would influence expression levels, protein stability, and/or the immune response to spike. All spike antigens contained a mutated furin cleavage site (RRAR mutated to a single alanine) plus two proline mutations at residues 986 and 987, which stabilize the spike trimer in the prefusion conformation.[3,49] Previous work has shown that stabilization of the prefusion conformation of other coronavirus spikes enhances protein expression and leads to greater neutralizing titers in the context of immunization;[50,51] thus, both vaccine and serology efforts involving soluble SARS-CoV-2 spike have utilized a stabilized form of the trimer.

For comparison, we also produced two spike ectodomain proteins fused to a trimeric coiled-coil, GCN4-pI$_Q$I[46] (denoted S-GCN4 and SΔC-GCN4; Figure 1). SΔC-GCN4 contained a deletion of residues 1138−1143 (which were present in SΔC-Fer) to eliminate a short helical segment prior to the start of the GCN4-pI$_Q$I coiled-coil. A similar truncated version of the spike trimer was recently utilized for antibody discovery.[5] We included the SARS-CoV-2 spike receptor binding domain (RBD; Figure 1) in our antigen panel because there is interest in employing the RBD as a potential vaccine candidate.[49,52,53]

Spike Ferritin Nanoparticles Can Be Expressed in Mammalian Cells and Purified to Homogeneity. The SARS-CoV-2 spike is a heavily glycosylated trimeric protein that can be challenging to produce recombinantly.[3,49,54] Production of recombinant spike ectodomain is commonly done in mammalian cell culture systems in which the protein is glycosylated during synthesis.[54] We expressed the spike ferritin nanoparticles using human Expi293F cells. Since the ferritin subunit facilitates self-assembly of the nanoparticles, production of purified spike-functionalized particles was achieved by transfecting a single plasmid followed by a two-step chromatographic purification (Figure 2A). After Expi293F transfection, we monitored expression levels of the four spike-based antigens (ferritins and trimers) with Western blots of cell culture supernatants probed with SARS-CoV-2 reactive monoclonal antibodies (mAbs) CR3022,[55−57] CB6,[58] and COVA2-15[5] (Figure S1A). Although fusing spike to ferritin

https://dx.doi.org/10.1021/acscentsci.0c01405
ACS Cent. Sci. 2021, 7, 183−199

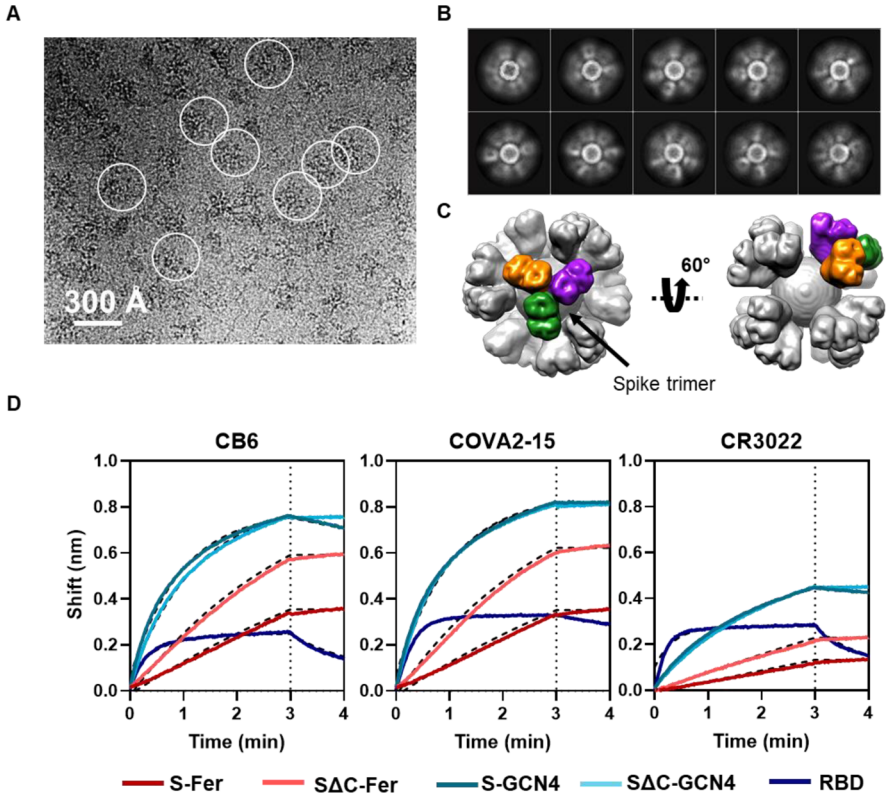

Figure 3. Cryo-EM and BLI confirm that spike proteins are presented on the particle surface with mAb epitopes intact. (A) Representative motion-corrected cryo-EM micrograph of the SΔC-Fer nanoparticles. Circles indicate representative particles that were picked for further analysis. Micrographs demonstrate that particles are approximately 300 Å. (B) Reference-free 2D class averages of SΔC-Fer. 2D class averages confirm the presence of both ferritin particles and the display of spike on the surface seen as density surrounding the particles. (C) Reconstructed cryo-EM map of the SΔC-Fer nanoparticle in two views. A single spike trimer on the surface is highlighted with each protomer of the trimer shown in a different color. (D) BLI binding of SARS-CoV-2 mAbs to purified spike antigens. Antigens were diluted to 100 nM monomer concentration (100 nM RBD, 33.3 nM S-GCN4 and SΔC-GCN4 trimer, and 4.2 nM S-Fer and SΔC-Fer 24-mer ferritin particle). Binding of all antigens to three SARS-CoV-2 reactive mAbs indicates that spike ferritin nanoparticles display epitopes similarly to the RBD and spike trimers. Curves were fitted with an association/dissociation nonlinear regression, and fits are represented with dashed black lines; k_{on} values for each binding reaction are shown in Figure S4A. Both S-Fer and SΔC-Fer exhibited a slight increase in signal during the dissociation step, perhaps due to rearrangements of the particles on the BLI sensor tip due to the extensive avidity present on the multimerized particles. Lack of binding to an off-target Ebola-specific antibody (ADI-15731) is presented in Figure S4B. Binding experiments were performed in at least duplicate; a representative trace and fit are shown from one replicate.

increases the size of the antigen from ∼450 kDa (trimer) to ∼4 MDa (ferritin), the expression levels for all spike proteins were comparable (Figure S1A). Nanoparticles can sometimes remain intact during SDS-PAGE analysis, even under denaturing conditions, which can lead to retention of some sample within the well, causing the intensity of the monomer band to appear weaker. Therefore, for a more quantitative estimate of the protein levels in Expi cell culture supernatant, we quantified the expression levels of each spike antigen using a dot blot of unpurified cell culture supernatant blotted with SARS-CoV-2 mAb CR3022. We made standard curves of purified antigen and compared these curves to expression levels from cell culture supernatants from a set (n = 5) of small-scale protein expressions (Figure S1B).[59] This analysis indicated similar expression trends to those observed via Western blot and further confirmed that fusion of spike to *H. pylori* ferritin did not impact expression levels. Interestingly, it also suggests that fusion of SΔC to ferritin enhances the levels of protein expression under these conditions.

Since the spike ferritin particles lack an affinity purification tag, we purified them to homogeneity using anion exchange followed by size-exclusion chromatography (Figure 2A). We used SEC-MALS to assess sample quality and homogeneity following purification.[60] No evidence of aggregation was detected from the S-Fer or the SΔC-Fer samples via ultraviolet absorbance (A280) or light scattering signals (Figure 2B). Additionally, we determined that a freeze−thaw cycle does not perturb particle formation or cause sample aggregation (Figure S2A). We used the light scattering and refractive index data from spike nanoparticles to determine (Figure S2B) molecular weights of 4.2 MDa (S-Fer) and 3.1 MDa (SΔC-Fer). These values are close to those expected from the amino acid sequences and the additional mass[61] expected from ∼20 predicted N-linked glycosylation sites (Figure S2B). Taken together, these experiments confirm that functionalization of *H. pylori* ferritin with the SARS-CoV-2 spike did not perturb assembly of the nanoparticles.

We also produced the S-GCN4, SΔC-GCN4, and RBD in human Expi293F cells. We purified these samples using NiNTA purification followed by size-exclusion chromatography and confirmed sample purity and homogeneity using SEC-MALS (Figure S2C). We observed a main peak and a secondary peak for the S-GCN4 sample, which has also been noted in other recently reported work describing expression

https://dx.doi.org/10.1021/acscentsci.0c01405
ACS Cent. Sci. 2021, 7, 183−199

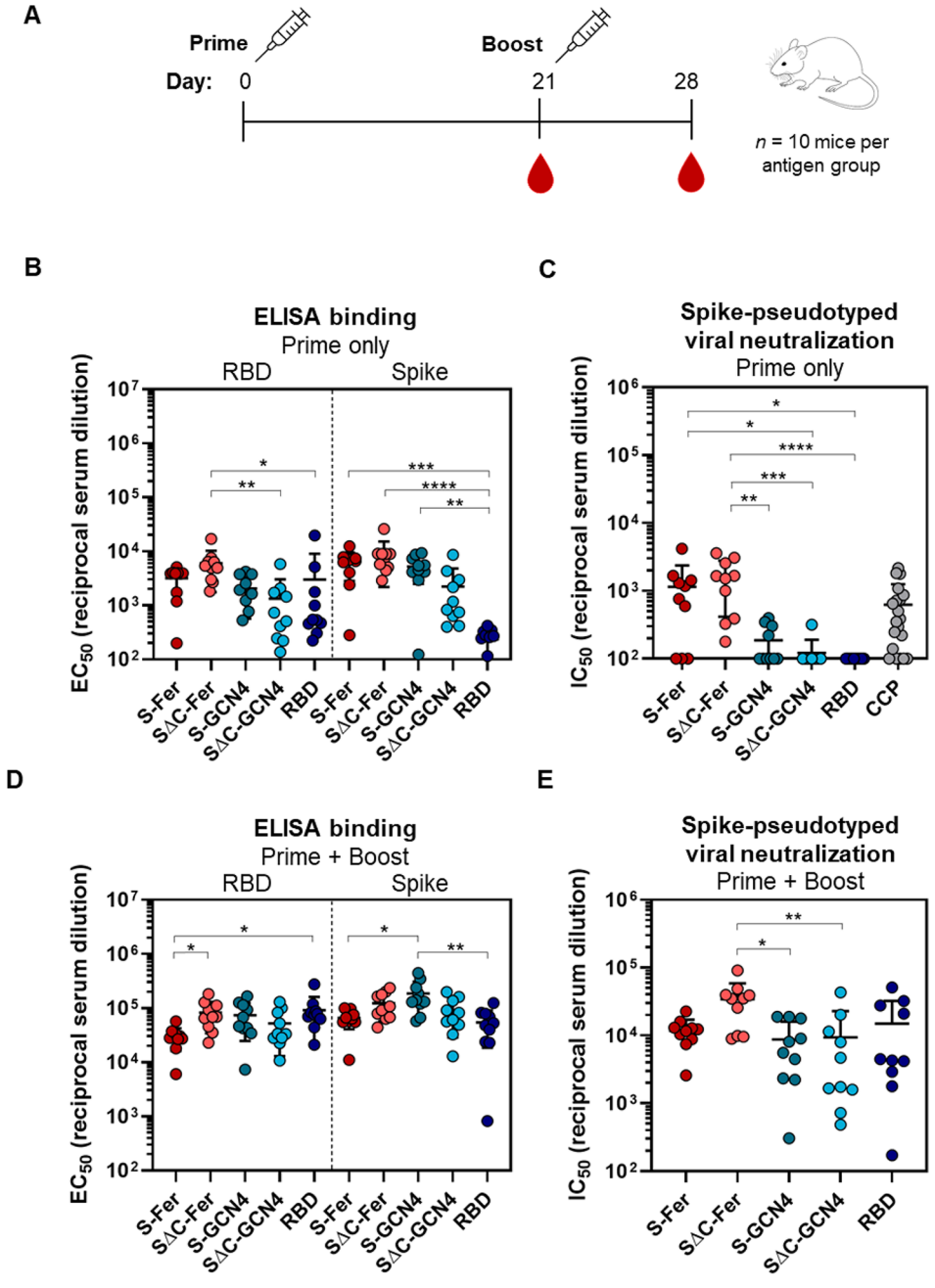

Figure 4. Immunization with SΔC-Fer nanoparticles elicits a stronger neutralizing response than immunization with nonferritin groups in mice. (A) Immunization schedule including a priming dose with 10 μg of antigen at day 0 and a boost with 10 μg of antigen at day 21. Serum was collected on days 0, 21, and 28. Both doses were adjuvanted with 10 μg of Quil-A and 10 μg of MPLA in a total volume of 100 μL per mouse administered via subcutaneous injection. (B) ELISA binding titers to both the RBD and full-length spike ectodomain after a single dose of antigen demonstrate that all groups elicited a SARS-CoV-2-directed antibody response following immunization. Each point represents the EC_{50} titer from a single animal; each bar represents the mean EC_{50} titer from the group (n = 10 mice per group). Error bars represent standard deviation. Points with signal less than EC_{50} 1:100 dilution are placed at the limit of quantitation for the assay. (C) S-Fer and SΔC-Fer antigens elicit stronger neutralizing antibody responses than spike trimers alone or RBD, as indicated by spike-pseudotyped lentivirus neutralizing titers after a single dose of antigen. Immunization with a single dose of S-Fer or SΔC-Fer elicits neutralizing responses that are at least 2-fold greater on average than those found in plasma from 20 convalescent COVID-19 patients (CCP). Each point represents the IC_{50} titer from a single animal or patient; each bar represents the mean IC_{50} titer from each group (n = 10 per group, with the exception of CCP which is n = 20). Error bars represent standard deviation. Samples with neutralizing activity that was undetectable at 1:50 dilution or with an IC_{50} less than 1:100 dilution are placed at the limit of quantitation. (D) ELISA binding titers to the RBD and spike after two doses of antigen show that the SARS-CoV-2-specific response against both antigens was boosted in all groups. Groups and error are as defined in part B. (E) Spike-pseudotyped lentivirus neutralization following two doses of antigen indicates that although all groups had a neutralizing response following two doses, animals immunized with SΔC-Fer have the highest neutralizing titers, and these are significantly greater than S-GCN4 and SΔC-GCN4. Groups and error are as defined in part C. Statistical comparisons for panels B–E were performed using Kruskal–Wallis ANOVA followed by Dunn's multiple comparisons. All p values are represented as follows: * = $p \leq 0.05$, ** = $p \leq 0.01$, *** = $p \leq 0.001$, **** = $p \leq 0.0001$. Mean titers with standard deviation and values from pairwise comparisons between groups can be found in Tables S1–S3.

https://dx.doi.org/10.1021/acscentsci.0c01405
ACS Cent. Sci. 2021, 7, 183–199

and purification conditions of spike trimers.[62] These populations may correspond to conformational populations of the trimer and have been suggested to potentially be related to RBDs on different protomers in "up" and "down" states.[3,7,62]

Structural and Functional Analysis Demonstrates That Spike-Functionalized Nanoparticles Are Stably Folded and Properly Display Epitopes of Interest. To confirm that spike is displayed on the surface of ferritin, we performed cryo-EM on both S-Fer and SΔC-Fer. Cryo-EM raw images showed observable densities around ferritin particles (Figure 3A and Figure S3A), indicating proper formation of the nanoparticles and display of spike on the surface. The two-dimensional class averages further showed the densities of spike surrounding ferritin (Figure 3B and Figure S3B). We chose to perform additional data collection and image processing of the SΔC-Fer particles since they had more defined spike density than the S-Fer particles. Using single-particle analysis, we determined the three-dimensional (3D) structure of the SΔC-Fer complex from ∼60 000 particles and achieved overall resolutions of 13.5 and 23.6 Å, with and without octahedral symmetry applied, respectively (Figure S3C−E). The overall shapes of the two cryo-EM maps were very similar, with a cross-correlation coefficient of 0.99 (Figure S3D,E). The map obtained with octahedral symmetry can be seen in two different views in Figure 3C. One representative trimer on the surface is highlighted, with each protomer indicated in a separate color to demonstrate the display of trimeric spike on the surface of ferritin.

The smearing of the spike protein densities (Figure 3B and Figure S3B) is likely due to the flexibility of spike on the ferritin surface resulting from the Ser-Gly-Gly linker (Figure 1). This conclusion predicts that density for the ferritin core of the nanoparticles would not be smeared. Indeed, when single-particle analysis of the SΔC-Fer cryo-EM data set focused on only the ferritin core, excluding spike-specific density, we were able to obtain a 3.7 Å resolution structure of the ferritin core of SΔC-Fer (Figure S3F).

Since we aimed to use the S-Fer and SΔC-Fer nanoparticles as antigens for eliciting SARS-CoV-2-directed antibodies, we confirmed that they displayed properly folded spike that could recognize mAbs and ACE2. We used BLI (Figure 3D) to assess binding of three SARS-CoV-2 mAbs (CR3022, COVA2-15, and CB6) in IgG form to S-Fer and SΔC-Fer. We performed the BLI experiments at a set concentration of 100 nM monomer for each antigen which corresponds to 100 nM RBD monomer, 33.3 nM S-GCN4 and SΔC-GCN4 trimer, and 4.2 nM S-Fer and SΔC-Fer 24-mer ferritin nanoparticle. Thus, observed differences in the magnitude of binding are largely due to differences in molar concentration of antigen. We fit the BLI data using an association/dissociation nonlinear regression and extracted k_{on} values for each mAb binding each antigen (Figure S4A). We could not obtain k_{off} values for a subset of the binding interactions due to the undetectable dissociation of IgGs from the highly avid spike ferritin nanoparticle samples (Figure 3D). Thus, we did not determine K_D values for mAbs binding to each antigen but used the k_{on} values as a metric to compare binding (Figure S4A). The mAbs bound the functionalized nanoparticles similarly to both the spike trimers and the RBD (Figure 3D and Figure S4A), confirming that display of the spike on ferritin nanoparticles does not perturb or occlude critical conformation-specific epitopes. We observed minimal binding when a nontarget mAb (anti-Ebola glycoprotein mAb, ADI-15731[63]) was loaded on the tip (Figure S4B). We also compared binding of the three mAbs as well as the ectodomain of human ACE2, the SARS-CoV-2 receptor, to all antigens using enzyme-linked immunosorbent assays (ELISAs; Figure S5). These ELISA results were consistent with those from BLI, indicating that SARS-CoV-2 and ACE2 bind the spike-functionalized particles as well as they bind spike trimers and RBD.

Immunization with Spike-Functionalized Nanoparticles Elicits SARS-CoV-2 Neutralizing Antibodies with a Single Dose. To assess the immune response to S-Fer and SΔC-Fer nanoparticles versus the other antigens, we immunized 10 mice (n = 5 in two replicate immunizations) with 10 μg of antigen adjuvanted with 10 μg of Quil-A and 10 μg of monophosphoryl lipid A (MPLA).[64−66] We collected serum at day 21 to assess the response to a single dose of antigen. We administered a second dose of antigen at day 21 and subsequently collected serum at day 28 to determine how the initial response to each antigen was boosted (Figure 4A). Mean ELISA titers and spike-pseudotyped lentivirus neutralization titers for all antigen groups at day 21 and day 28 can be found in Table S1.

After a single dose ("Prime only"), all groups exhibited a detectable antibody response against both RBD and spike, as revealed by ELISA (Figure 4B). To analyze neutralizing titers, we used lentivirus pseudotyped with SARS-CoV-2 spike[47] and assessed inhibition of viral entry into HeLa cells overexpressing ACE2.[48] Neutralization with pseudotyped viruses is a common way to assess viral inhibition in a BSL2 setting since the SARS-CoV-2 replicating pathogen requires a BSL3 facility.[47,67] We validated the neutralization assay using published neutralizing mAbs against SARS-CoV-2 (Figure S6).

Analysis of antisera from immunized mice revealed that the only groups with notable neutralizing activity after a single dose of antigen were those immunized with S-Fer or SΔC-Fer (Figure 4C), underscoring that multivalent presentation greatly enhances the neutralizing antibody response in a single-dose regimen of an adjuvanted SARS-CoV-2 subunit vaccine. As illustrated in Figure 4C, the SΔC-Fer group had significantly higher neutralizing titers than all three nonferritin groups at the day 21 time point, whereas the S-Fer group elicited significantly greater neutralizing responses than SΔC-GCN4 and RBD. Importantly, antisera from mice immunized with a single dose of either S-Fer or SΔC-Fer had ∼2-fold higher mean neutralizing titers than those observed in a cohort of 20 convalescent COVID-19 plasma donors (Figure 4C, far right).

The lack of neutralizing titers after a single-dose immunization in both the RBD and SΔC-GCN4 groups and minimal neutralizing titers in the S-GCN4 group (Figure 4C) are consistent with recent reports that also found that a single dose of spike trimer or RBD was insufficient to elicit robust neutralizing antibodies in mice.[31,32,68] Consistent with the lentiviral neutralization results (Figure 4C), the only two groups with substantial ACE2-competing antibodies (as determined by a decrease in ACE2 binding to RBD on ELISA) were those immunized with spike ferritin nanoparticles (Figure S7, left). ACE2-blocking activity in the antisera of mice after a single dose of antigen (day 21) appeared to be weak, as even the nanoparticle groups with the strongest neutralizing response exhibited minimal blocking at the highest serum concentration tested (1:50 dilution), and no groups exhibited any blocking activity at a 1:500 dilution (Figure S7).

https://dx.doi.org/10.1021/acscentsci.0c01405
ACS Cent. Sci. 2021, 7, 183−199

To evaluate the effect of boosting on the immune responses to these antigens, we administered a second dose of antigen on day 21 and collected serum at day 28 ("Prime + Boost"). We analyzed the post-boost serum for RBD and spike titers, ACE2 blocking activity, and neutralization potency. The immune response to all antigens was increased, and antigen-specific titers for both RBD and spike were similar among groups after the second dose (Figure 4D). ACE2 blocking activity was notably enhanced after the boost, and all five antigen groups had nearly complete ACE2 blocking at 1:50 serum dilution at that time point (Figure S7, right). While all antigen groups also had partial ACE2 blocking activity at 1:500 serum dilution, the levels of ACE2 blocking at this dilution did not relate to overall trends in neutralizing titers (compare Figure 4E and Figure S7). This discordance indicates that ACE2-blocking activity may not correlate with neutralizing titers for some antigens and suggests that neutralizing epitopes other than the ACE2 binding site exist on the SARS-CoV-2 spike (see refs 5 and 69).

To assess the polarization of the immune response following two doses of antigen, we quantified the levels IgG1, IgG2a, and IgG2b titers for RBD-specific antibodies (Figure S8). IgG subclasses can provide information regarding whether a given response is biased toward a Th1- or Th2-like response.[70−73] Adjuvants are known to play a major role in influencing the polarization of vaccine immune responses, and prior work has shown that Quil-A and MPLA adjuvants can lead to a Th1-biased response.[70,71] Some vaccine candidates against SARS-CoV were found to cause pulmonary immunopathology potentially due to Th2-type responses in small animal models,[74−77] and thus one focus for SARS-CoV-2 vaccine development has been to favor a Th1-type response.[72,73] A comparison of the ratio of IgG2a/IgG1 antibody titers among antigen groups demonstrated that, except for the RBD, the antigens exhibit a balanced IgG2a and IgG1 response, which was slightly skewed toward IgG2a for both the SΔC-Fer and S-GCN4 groups (Figure S8A,B). Notably, the RBD elicited a substantially higher IgG1 response as compared to both IgG2a and IgG2b, suggesting that this antigen in combination with Quil-A/MPLA caused a Th2-biased immune response (Figure S8B,C). IgM responses did not substantially differ among antigen groups at the day 28 time point and were lower than IgG isotypes (Figure S8D), and at the same time point serum IgA levels were undetectable (data not shown).

Given that each antigen contains a non-SARS-CoV-2 fragment, we wanted to assess the off-target antibody responses directed at either the *H. pylori* ferritin, the GCN4 trimerization domain, or the His-tag. We observed anti-*H. pylori* ferritin responses in the S-Fer and SΔC-Fer groups that were similar and were equivalent to or less than anti-RBD and anti-spike titers from the same groups as determined by ELISA (Figure S9, left). The S-GCN4 and SΔC-GCN4 groups had similar anti-GCN4 responses (Figure S9, middle), suggesting that the *H. pylori* ferritin and GCN4 domains are equivalently immunogenic. Interestingly, when we probed the anti-His-tag response specifically, we observed that the SΔC-GCN4 group had a notably higher His-tag response as compared to either the S-GCN4 or the RBD group, even though all three antigens contained His-tags (Figure S9, right). This could suggest that this antigen either was less structurally stable or had other antigenic features that altered the overall immunogenicity to cause a higher tag-directed response. Additionally, this indicates that, for the RBD- and spike-specific titers from the S-GCN4, SΔC-GCN4, and RBD groups, the His-tag on the plated antigen likely did not impact the overall titers for the S-GCN4 and RBD groups but may have slightly increased the titers for the SΔC-GCN4 group.

Though antisera from all groups exhibited neutralizing activity after a boost, mice immunized with SΔC-Fer exhibited the highest neutralizing titers overall and had significantly higher titers than both the S-GCN4 and SΔC-GCN4 groups (Figure 4E). Importantly, the variation in response to the nonferritin groups was also considerably larger than the variability detected in mice immunized with S-Fer or SΔC-Fer nanoparticles (Figure 4E), suggesting that the multivalent presentation of spike facilitated a more consistent immune response. Furthermore, the neutralizing antibody response elicited by SΔC-Fer shows dose-dependent trends (Figure S10A). Though a decrease in dose from 10 to 1 μg led to an increased variability in the elicitation of neutralizing titers, the presence of neutralizing antibodies in a subset of mice following only 1 μg of SΔC-Fer could have important dose-sparing implications. Additionally, neutralizing titers remain stable even to 20 weeks following a single immunization with 20 μg (Figure S10B), demonstrating that this formulation may successfully achieve neutralizing antibody levels that persist in the months following vaccination. These data demonstrate that the spike ferritin nanoparticles presented here, particularly SΔC-Fer, are superior vaccine candidates to spike trimer or RBD alone.

DISCUSSION

Global management of the COVID-19 pandemic depends not only upon the development of safe and protective vaccine candidates but also on the rapid production and deployment of billions of doses. Given these extensive manufacturing challenges, vaccination strategies requiring only a single dose could be critical to achieving worldwide immunization against SARS-CoV-2. Toward this end, we designed and characterized two vaccine candidates based on ferritin nanoparticles (S-Fer and SΔC-Fer) that display multiple copies of the SARS-CoV-2 spike and can be readily expressed in mammalian cells. These proteins can be purified using routine methods and a production scheme similar to that for soluble spike trimers.

Immunization with the spike nanoparticles elicited neutralizing antibodies in mice after a single dose, whereas immunization with the RBD or spike trimers elicited little to no neutralizing titers with the same dose (Figure 4C). Interestingly, deletion of the C-terminal portion of the spike ectodomain enhanced the neutralizing antibody response specifically in the context of the nanoparticle (Figure 4C). After a second dose, all antigen groups elicited neutralizing antibodies; however, the SΔC-Fer immunized mice had the highest overall neutralizing titers and, importantly, had significantly higher titers than both the S-GCN4 and SΔC-GCN4 trimer groups (Figure 4E). These results provide important insight into the use of spike ferritin nanoparticles as an effective single-dose vaccine against SARS-CoV-2.

Ferritin nanoparticles are of significant interest for developing new vaccines because they self-assemble into stable structures that display trimeric proteins on 3-fold symmetry axes.[39] Unlike nanoparticle platforms that require postpurification conjugation of an antigen to a carrier or scaffold,[78] here, spike-functionalized nanoparticles were produced by transfecting a single plasmid encoding the spike fused to the ferritin subunit into mammalian cells. We built on existing

https://dx.doi.org/10.1021/acscentsci.0c01405
ACS Cent. Sci. 2021, 7, 183−199

work using ferritin nanoparticles to display other viral antigens for vaccine development[30,33−38] and designed nanoparticles displaying the SARS-Cov-2 spike ectodomain. Importantly, the two ferritin-based antigens that we designed (S-Fer and SΔC-Fer) expressed comparably to spike trimers (S-GCN4 and SΔC-GCN4) in mammalian cells (Figure S1), indicating that fusing the spike to ferritin does not negatively impact protein production. As glycosylation can influence proper folding of viral antigens, it is also noteworthy that expression was achieved in mammalian cells, which allows spike proteins to be produced with native-like glycosylation.[54]

These constructs could also be important for the development of nucleic acid vaccines given the self-assembly of spike ferritin nanoparticles following production in mammalian cells, expression levels comparable to those of spike trimers, and the enhanced immune response after a single dose of antigen. We administered equivalent doses of spike ferritin nanoparticle and trimer and observed an enhanced response after single-dose and two-dose vaccine regimens with the SΔC-Fer (Figure 4C,E). Thus, administration of a nucleic acid vaccine encoding a multimerized ferritin-based spike protein could potentially elicit a heightened response versus constructs encoding spike alone, although we did not test that hypothesis here.

Following purification of the spike-functionalized nanoparticles from Expi293F culture supernatant, we extensively characterized their biophysical properties to ensure that the spikes were properly folded and stable and could display important epitopes of interest. We confirmed the structure, homogeneity, and epitope conformations of spike-functionalized nanoparticles using cryo-EM (Figure 3A−C and Figure S3), SEC-MALS (Figure 2B and Figure S2), and BLI-measured binding to conformation-specific SARS-CoV-2 mAbs (Figure 3D).

Remarkably, mice immunized with a single dose of either S-Fer or SΔC-Fer elicited mean neutralizing antibody titers that were approximately 2-fold higher than mean titers observed in plasma from convalescent COVID-19 patients (Figure 4C). Additionally, mice immunized with one dose of SΔC-Fer had significantly higher neutralizing titers versus all nonferritin groups, whereas mice immunized with one dose of S-Fer had significantly higher titers than the RBD and SΔC-GCN4 group (Figure 4C). These data clearly demonstrate that equivalent doses of spike ferritin nanoparticles elicit a better neutralizing response versus RBD or trimer alone in a single-dose setting which is consistent with observations from other recent studies investigating other multimerized SARS-CoV-2 vaccine platforms.[31,32] A comparison of neutralizing antibody titers observed in these other studies reveals that, despite the use of different adjuvants, the spike ferritin nanoparticles we present here elicit similar levels of neutralizing antibodies following one or two doses.[31,32]

Mice immunized with the RBD exhibited no observable serum neutralizing activity after a single dose (Figure 4C) despite having RBD-specific antibody titers that were similar to those in other groups (Figure 4B). This discordance suggests that RBD binding titers may not be a strong correlate of neutralizing antibody responses in the context of vaccination, particularly for candidates based on the RBD alone.[52,79,80] Notably, the full-length spike ELISA binding titers from animals immunized with the RBD were significantly lower than titers from the other groups (Figure 4B), suggesting that immunization with monomeric RBD elicits antibodies to epitopes that are occluded in full-length spike, rendering them unable to neutralize virus. This supports the notion that the response to RBD may have largely focused on the non-neutralizing regions.

After a second dose of antigen, all antigens elicited detectable neutralizing antibody titers (Figure 4E). Despite the lack of detectable neutralizing signal in the RBD or SΔC-GCN4 groups after a single dose (Figure 4C), these groups exhibited titers roughly equivalent to those of the S-GCN4 group after a second dose (Figure 4E). Interestingly, mice immunized with either S-Fer or SΔC-Fer had less variability in response than the other three groups (Figure 4E), suggesting that multivalent presentation facilitates more consistent elicitation of neutralizing antibodies. Although all groups elicited a neutralizing response after the second dose, the mice immunized with SΔC-Fer had the highest overall neutralizing titers and elicited significantly higher neutralizing titers versus both spike trimers tested (Figure 4E). Taken together, these data suggest that SΔC-Fer is the best-performing antigen out of those we tested here and could be a favorable candidate for use in a subunit or nucleic acid vaccine against SARS-CoV-2.

Effective global deployment of a SARS-CoV-2 vaccine will depend on several logistical factors. The number of doses in an immunization regimen required to achieve efficacy will be of critical importance due to the number of doses required worldwide and to the ability to access patients multiple times. Therefore, assessing candidates that can achieve protection after a single dose is highly important for implementing a global vaccination strategy. Here, we have demonstrated that a dose of either S-Fer or SΔC-Fer nanoparticles adjuvanted with Quil-A and MPLA was sufficient to achieve neutralizing titers greater than those in plasma from convalescent COVID-19 patients. Additionally, both S-Fer and SΔC-Fer form nanoparticles spontaneously following expression in mammalian cells without the need for a conjugation step, showcasing the potential application of spike ferritin constructs to nucleic acid-based vaccine strategies. Taken together, our data indicate that the multivalent presentation of the SARS-CoV-2 spike is an effective way to enhance the antibody response after a single dose, providing key insight for the development of an effective and deployable vaccine to combat the COVID-19 pandemic.

MATERIALS AND METHODS

DNA Plasmid Construction and Propagation. All spike constructs were cloned from a full-length spike expression plasmid received from Dr. Florian Krammer.[49] This construct contains residues 1−1213 from the Wuhan-Hu-1 genome sequence (GenBank MN9089473), followed by a thrombin cleavage site, a T4 fibritin trimerization domain, and a hexahistidine tag for purification. This construct was cloned out of the parent vector and into an in-house pADD2 mammalian expression vector using HiFi PCR (Takara) followed by In-Fusion (Takara) cloning with *Eco*RI/XhoI cut sites. This construct was used to clone subsequent spike ferritin and spike GCN4-pI$_Q$I trimer constructs. Full-length spike ferritin (S-Fer) and spikeΔCferritin (SΔC-Fer) were cloned by polymerase chain reaction (PCR) amplification of full-length spike (residues 1−1213) or spikeΔC (residues 1−1143) off the parent expression vector. This was followed by a stitching PCR in which constructs were annealed to an amplicon containing *H. pylori* ferritin (residues 5−168) originally generated as a gene-block fragment from Integrated DNA Technologies (IDT). The spike and ferritin subunits were separated by a SGG linker.[33] Spike ferritin amplicons were inserted into the

https://dx.doi.org/10.1021/acscentsci.0c01405
ACS Cent. Sci. 2021, 7, 183−199

pADD2 mammalian expression vector via In-Fusion using *Eco*RI/XhoI cut sites. The spike trimer constructs were cloned similarly and fused to the GCN4-pI$_Q$I[46] domain instead of ferritin. The spikeΔC trimer included residues 1−1137 followed by a glycine residue and then the GCN4-pI$_Q$I domain. The full-length spike trimer included residues 1−1213 followed by a GGGGS linker and then the GCN4-pI$_Q$I domain. Both trimer constructs contained a hexa-histidine tag for NiNTA purification.

The SARS-CoV-2 RBD construct was kindly provided by Dr. Florian Krammer.[49] This construct contains the native signal peptide (residues 1−14) followed by residues 319−541 from the SARS-CoV-2 Wuhan-Hu-1 genome sequence (GenBank MN908947.3) and a hexa-histidine tag at the C-terminus for purification. This expression plasmid (pCAGGS) contains a CMV promoter for protein expression in mammalian cells.

The variable heavy chain (HC) and variable light chain (LC) sequences for SARS-CoV-2 reactive mAbs, CR3022 (HC GenBank DQ168569, LC Genbank DQ168570), CB6 (HC GenBank MT470197, LC GenBank MT470196), and COVA-2-15 (HC GenBank MT599861, LC GenBank MT599945) were codon optimized for human expression using the IDT Codon Optimization Tool and ordered as gene-block fragments from IDT. Fragments were PCR amplified and inserted into linearized CMV/R expression vectors containing the heavy chain or light chain Fc sequence from VRC01 using In-Fusion.

Soluble human ACE2 with an Fc tag was constructed by PCR amplifying ACE2 (residues 1−615) from Addgene plasmid 1786 (a kind gift from Dr. Jesse Bloom) and fusing it to a human Fc domain from VRC01, separated by a TEV-GSGG linker using a stitching PCR step. ACE2-Fc was inserted into the pADD2 mammalian expression vector via In-Fusion using *Eco*RI/XhoI cut sites.

After all cloned plasmids were sequence confirmed using Sanger sequencing, plasmids were transformed into Stellar Cells (Takara) and grown overnight in 2xYT/carbenicillin cultures, with the exception of the CMV/R mAb plasmids which were grown in 2xYT/kanamycin cultures. Plasmids were prepared for mammalian cell transfection using Machery Nagel Maxi Prep columns. Eluted DNA was filtered in a biosafety hood using a 0.22 μm filter prior to transfection.

Expression and Purification of SARS-CoV-2 Antigens, mAbs, and Soluble ACE2. All antigens for immunization, mAbs, and soluble human ACE2-Fc were expressed and purified from Expi293F cells. Expi293F cells were cultured using 66% FreeStyle 293 Expression/33% Expi293 Expression medium (ThermoFisher) and grown in polycarbonate baffled shaking flasks at 37 °C and 8% CO_2 while shaking at 120 rpm. Cells were transfected at a density of approximately (3−4) × 10^6 cells/mL. Transfection mixtures were made by adding 568 μg of maxi-prepped DNA to 113 mL of culture medium (per liter of transfected cells) followed by addition of 1.48 mL of FectoPro (Polyplus). For mAbs, cells were transfected with a 1:1 ratio of HC:LC plasmid DNA. Mixtures were incubated at room temperature for 10 min and then added to cells. Cells were immediately boosted with D-glucose (4 g/L final concentration) and 2-propylpentanoic (valproic) acid (3 mM final concentration). Cells were harvested 3−5 days post-transfection via centrifugation at 7000*g* for 15 min. Culture supernatants were filtered with a 0.22 μm filter.

Superfolder GFP (sfGFP) was tagged with either GCN4-Avi-His (GCN4 tag domain amino acid sequence taken from[81]) or His-tag only to quantify off-target tag antibody responses. sfGFP-His and sf-GFP-GCN4-His encoded in pET28a bacterial T7-expression vectors were transformed into BL21 cells and induced at OD 0.6 with 1 mM isopropyl β-D-1-thiogalactopyranoside (IPTG) for 3 h at 37 °C. Cells were harvested by spinning at 7000*g* for 10 min, resuspended in 10 mM imidazole/1× PBS [pH 7.4], lysed by sonicating for 20 s three times, and spun at 15 000*g* for 20 min following lysis. sfGFP-His and sf-GFP-GCN4-His were then purified from supernatants using NiNTA resin as described below.

S-Fer, SΔC-Fer, and WT *H. pylori* ferritin nanoparticles were isolated using anion-exchange chromatography followed by size-exclusion chromatography using an SRT SEC-1000 (Sepax) column. Briefly, Expi293F culture supernatants were concentrated using tangential flow filtration with a GE AKTA Flux S with a 10 kDa molecular weight cutoff (MWCO) hollow fiber cartridge (UFP-10-E-4MA) and then buffer-exchanged into 20 mM Tris [pH 8.0] via overnight dialysis at 4 °C using 100 kDa MWCO dialysis tubing. For some preps, culture supernatant was dialyzed directly and not concentrated using tangential flow filtration. Dialyzed culture supernatants were filtered through a 0.22 μm filter and loaded onto a 5 mL HiTrapQ anion-exchange column (GE) equilibrated in 20 mM Tris [pH 8.0] on a GE AKTA Pure system. Ferritin nanoparticles were eluted with a sodium chloride (NaCl) gradient, and the particle-containing fractions were identified via Western blot with CR3022 for spike ferritins or SDS-PAGE followed by staining with GelCode blue stain reagent (Thermo) for WT *H. pylori* ferritin. Fractions were pooled and concentrated using a 100 kDa MWCO Amicon spin filter and subsequently purified on a GE AKTA Pure system using an SRT SEC-1000 SEC column equilibrated in 1× Dulbecco's phosphate-buffered saline (DPBS) (Gibco).

RBD, S-GCN4, SΔC-GCN4, sf-GFPHis, and sfGFP-GCN4-His were purified with HisPur NiNTA resin (ThermoFisher). Prior to purification, resin was washed 3× with ∼10 column volumes of wash buffer (10 mM imidazole/1× PBS [pH 7.4]). Expi293F cell culture supernatants were diluted 1:1 with 10 mM imidazole/1× PBS [pH 7.4]; resin was added to diluted cell supernatant and incubated at 4 °C. Resin/supernatant mixtures were agitated during binding using a stir-bar and a magnetic stir-plate. Resin/supernatant mixtures were added to glass chromatography columns for gravity flow purification. Resin was washed with 10 mM imidazole/1× PBS [pH 7.4], and proteins were eluted with 250 mM imidazole/1× PBS. NiNTA elutions were concentrated using Amicon spin concentrators (10 kDa MWCO for RBD, sfGFP-His, and sfGFP-GCN4-His and 100 kDa MWCO for spike trimers) followed by size-exclusion chromatography. The RBD, sfGFP-His, and sfGFP-GCN4-His were purified using a GE Superdex 200 Increase 10/300 GL column, and the S-GCN4 and SΔC-GCN4 proteins were purified using a GE Superose 6 Increase 10/300 GL column. Columns were pre-equilibrated in 1× Dulbecco's phosphate-buffered saline (DPBS) (Gibco) or 1× PBS [pH 7.4].

Fractions were pooled based on A280 signals and/or SDS-PAGE on 4−20% Mini-PROTEAN TGX protein gels stained with GelCode blue stain reagent (ThermoFisher). Samples for immunizations were supplemented with 10% glycerol, filtered through a 0.22 μm filter, snap frozen, and stored at −20 °C until use.

https://dx.doi.org/10.1021/acscentsci.0c01405
ACS Cent. Sci. 2021, 7, 183−199

mAbs and ACE2-hFc were purified using Protein A agarose resin (Pierce). Filtered cell culture supernatant was diluted 1:1 with 1× PBS [pH 7.4] and added to Protein A resin which was prewashed with ∼10 column volumes of 1× PBS [pH 7.4]. Resin/supernatant mixtures were batch bound at 4 °C. Proteins were eluted with 100 mM glycine [pH 2.8], and elutions were neutralized via addition of 1/10th volume 1 M Tris [pH 8.0].

Western Blot Analysis of Expi293F Culture Supernatants. Expi293F culture supernatants were collected 3 days after transfection, harvested via spinning at 7000*g* for 15 min, and filtered through a 0.22 μm filter. Samples were diluted in SDS-PAGE Laemmli loading buffer (Bio-Rad), boiled at 95 °C, and run on a 4−20% Mini-PROTEAN TGX protein gel (Bio-Rad). Proteins were transferred to nitrocellulose membranes using a Trans-Blot Turbo transfer system. Blots were blocked in 5% milk/PBST (1× PBS [pH 7.4], 0.1% Tween 20) and then washed with PBST. In-house-made primary antibodies CR3022, COVA2-15, and CB6 (approximate concentrations 0.8−1.3 mg/mL) were added at a 1:10 000 dilution in PBST. Blots were washed with PBST, and secondary rabbit antihuman IgG H&L HRP (abcam ab6759) was added at 1:10 000 in PBST. Blots were developed using Pierce ECL substrate and imaged using a GE Amersham imager 600.

Dot Blot Analysis of Expi293F Culture Supernatants. Purified proteins were diluted into conditioned expression medium (medium harvested 3 days post-mock-transfection) to a final concentration of 0.1 mg/mL and serially diluted 3-fold using conditioned medium as diluent. Dilution series were made in two independent replicates. Each concentration (2 μL) was dotted onto a nitrocellulose membrane to produce a standard curve. Expi293F culture supernatants from spike antigen expressions were harvested 3 days post-transfection via centrifugation at 7000*g* for 15 min and filtered through a 0.22 μm filter. Supernatants were spotted on the same blot as the standard curve. Blots were left to dry for 20 min in a fume hood and then blocked in 5% milk/PBST for 10 min at room temperature. CR3022 (4 μg) was added to blocking solution (0.4 μg/mL final concentration) and incubated for 1 h at room temperature. Blots were washed 16 times with 9 mL of PBST. Secondary antibody was added at 1:10 000 (abcam ab6759, rabbit antihuman IgG H&L HRP) in 5% milk/PBST and incubated for 1 h at room temperature. Blots were washed 16 times with 9 mL of PBST, developed using Pierce ECL Western blotting substrate, and imaged using a GE Amersham imager 600. Replicate protein expressions (n = 5) were performed and included in the analysis. Dots were quantified using the gel analysis protocol in Fiji (ImageJ), and curves were fitted using a linear regression in GraphPad Prism 8.4.1. Statistical analysis on expression data presented in Figure S1B was assessed using an ordinary one-way ANOVA with Tukey's multiple comparisons tests using GraphPad Prism 8.4.1. * = $p \leq 0.05$, ** = $p \leq 0.01$, *** = $p \leq 0.001$, **** = $p \leq 0.0001$.

SEC-MALS of SARS-CoV-2 Antigens. SEC-MALS was performed on an Agilent 1260 Infinity II HPLC with Wyatt detectors for light scattering (miniDAWN) and refractive index (Optilab). Purified antigen (1−10 μg) was loaded onto a Superdex 200 Increase 3.2/200 (RBD) or onto an SRT SEC-1000 4.6 × 300 mm (spike proteins) column equilibrated in 1× PBS [pH 7.4] or 1× Dulbecco's phosphate-buffered saline (DPBS) (Gibco). Columns were flowed at a rate of 0.15 mL/min (S200) or 0.35 mL/min (SRT SEC-1000). Molecular weights were determined using ASTRA 7.3.2 (Wyatt Technologies).

Cryo-EM Data Acquisition. Samples were diluted to a final concentration of ∼0.4 mg/mL for both the S-Fer and SΔC-Fer particles after purification. The samples (3 μL) were applied onto glow-discharged 200-mesh R2/1 Quantifoil grids coated with continuous carbon. The grids were blotted for 2 s and rapidly cryocooled in liquid ethane using a Vitrobot Mark IV instrument (Thermo Fisher Scientific) at 4 °C and 100% humidity. Samples were screened using a Talos Arctica cryoelectron microscope (Thermo Fisher Scientific) operated at 200 kV. The spikeΔC ferritin sample was imaged in a Titan Krios cryoelectron microscope (Thermo Fisher Scientific) operated at 300 kV with GIF energy filter (Gatan) at a magnification of 130 000× (corresponding to a calibrated sampling of 1.06 Å per pixel). Micrographs were recorded with EPU 2.6 (Thermo Fisher Scientific) with a Gatan K2 Summit direct electron detector; each image was composed of 30 individual frames with an exposure time of 6 s and an exposure rate of 7.8 electrons per second per Å^2. A total of 3684 movie stacks was collected.

Single-Particle Image Processing and 3D Reconstruction. All movie stacks were first imported into Relion 3.0.6[82] for image processing. Motion-correction was performed with MotionCor2 1.3.2,[83] and the contrast transfer function was determined with CTFFIND4 4.1.13.[84] All particles were autopicked using the NeuralNet option in EMAN2 2.31,[85] yielding 152 734 particles from 3540 selected micrographs. Then, particle coordinates were imported into Relion 3.0.6, where poor 2D class averages were removed through several rounds of 2D classification. The initial model was built in cryoSPARC[86] using the *ab initio* reconstruction option with octahedral symmetry applied. The final 3D refinement was performed using 62 837 particles with or without octahedral symmetry applied; a 13.5 Å map and a 23.6 Å map were obtained, respectively. Resolution for the final maps was estimated with the 0.143 criterion of the Fourier shell correlation curve. A Gaussian low-pass filter was applied to the final 3D maps displayed in the UCSF Chimera 1.13.1 software package.[87]

BLI of mAbs Binding to SARS-CoV-2 Purified Antigens. BLI was performed on an OctetRed 96 system (ForteBio). Antigens and mAbs were diluted in Octet buffer (0.5% bovine serum albumin, 0.02% Tween, 1× Dulbecco's phosphate-buffered saline (DPBS) (Gibco)) and plated in 96-well flat-bottom black plates (Greiner). Tips were pre-equilibrated in Octet buffer and regenerated in 100 mM glycine [pH 1.5] prior to binding antigens. Anti-Human Fc sensor tips (Forte) were dipped into 200 nM mAb and then submerged into wells containing 100 nM (protomer or monomer concentration) of each antigen. The final concentration of each antigen was as follows: 100 nM RBD monomer, 33.3 nM S-GCN4 and SΔC-GCN4 trimer, and 4.2 nM S-Fer and SΔC-Fer nanoparticle. Background subtraction was performed using an mAb-loaded sensor tip submerged into a well containing buffer only.

ELISA with Purified mAbs and Mouse Serum. ELISA of SARS-CoV-2 antigens was performed by coating antigens on MaxiSorp 96-well plates (ThermoFisher) at 2 μg/mL in 1× PBS [pH 7.4] overnight at 4 °C. Mouse serum ELISAs were performed using RBD or full-length spike ectodomain with a T4 fibritin (foldon) trimerization domain, described in detail in ref 49. ELISAs to quantify off-target antibody responses

https://dx.doi.org/10.1021/acscentsci.0c01405
ACS Cent. Sci. 2021, 7, 183−199

were performed by coating either WT *H. pylori* ferritin particles, sfGFP-GCN4-Avi-His (GCN4-Avi-His sequence taken from ref 81), or sfGFP-His. After coating, plates were washed 3× with PBST and blocked overnight at 4 °C with ChonBlock Blocking/Dilution ELISA buffer (Chondrex). ChonBlock was removed manually, and plates were washed 3× with PBST. Mouse serum samples, purified mAbs, and ACE2-Fc were serially diluted in diluent buffer (1× PBS, 0.5% bovine serum albumin, 2% filtered fetal bovine serum, 0.2% bovine gamma globulins (Sigma), 5 mM EDTA, 0.1% Tween) starting at 1:50 serum dilution or 10 μg/mL and then added to coated plates for 1 h at room temperature. Plates were washed 3× with PBST. For mouse serum ELISAs, HRP goat antimouse (BioLegend 405306) was added at a 1:10 000 dilution in diluent buffer for 1 h at room temperature. Isotyping experiments to quantify isotypes of RBD-specific antibodies were performed by adding a 1:10 000 dilution of either HRP antimouse IgG1 (abcam ab97240), HRP antimouse IgG2a heavy chain (abcam ab97245), HRP antimouse IgG2b heavy chain (abcam ab97250), HRP antimouse IgA alpha chain (abcam ab97235), or HRP antimouse IgM mu chain (abcam ab97230). For purified mAbs and ACE2-Fc, Direct-Blot HRP antihuman IgG1 Fc antibody (Biolegend 410604) was added at a 1:10 000 dilution in diluent buffer for 1 h at room temperature.

ACE2 blocking assays were performed by coating RBD as described for other antigens, incubating serially diluted mouse serum for 1 h at room temperature, and then adding ACE2-Fc at a final concentration of 1 μg/mL to wells for 1 h at room temperature. ACE2 binding was measured with Direct-Blot HRP antihuman IgG1 Fc at a 1:10 000 dilution, and blocking was quantified as the decrease in observed ACE2 binding as a function of serum dilution.

After incubation with secondary antibody, ELISA plates were washed 6× with PBST. Plates were developed for 6 min using One-Step Turbo TMB substrate (Pierce) and were quenched with 2 M sulfuric acid. Absorbance at 450 nm was determined using a BioTek plate reader. Background was determined using an average of wells containing no serum, mAb, or ACE2. This value was then subtracted from all wells on the plate. Background subtracted values were then imported into GraphPad Prism 8.4.1 and fitted with a three-parameter nonlinear regression to obtain EC_{50} or apparent K_D values.

For ACE2 blocking assays, A450 values from ACE2 only wells and background wells (no serum, no ACE2) were averaged and set at either 0% ACE2 blocking (ACE2 only) or 100% ACE2 blocking (background). A450 values for each serum concentration were then normalized in GraphPad Prism 8.4.1 using these values. Percent ACE2 blocking at either 1:50 or 1:500 serum dilution can be found in Figure S6 for both day 21 and day 28 immunization time points.

Mouse Immunizations. Balb/c female mice (6−8 weeks old) were procured from The Jackson Laboratory. All mice were maintained at Stanford University according to the Public Health Service Policy for "Humane Care and Use of Laboratory Animals" following a protocol approved by Stanford University Administrative Panel on Laboratory Animal Care (APLAC-33709). Mice were immunized via subcutaneous injection of 10 μg of antigen with the exception of SΔC-Fer dosing and longevity studies in which animals were immunized with either 0.1, 1, 10, or 20 μg as specified in Figure S10. All antigen doses were formulated with 10 μg of Quil-A (InVivogen) and 10 μg of monophosphoryl lipid A (InVivogen) diluted in 1× Dulbecco's phosphate-buffered saline (DPBS) (Gibco) in a total volume of 100 μL per injection. Mice were immunized at day 0 and day 21. Serum was collected at days 0, 21, and 28 and processed using Sarstedt serum collection tubes. Day 0 serum was analyzed for both ELISA binding and lentiviral neutralization and showed no evidence of binding or neutralizing activity (data not shown).

Collection of Plasma from Convalescent COVID-19 Patients. Convalescent COVID-19 plasma (CCP) donor samples were obtained from residual ethylenediaminetetraacetic acid (EDTA) specimens at the time of collection, aliquoted, and stored at −80 °C. CCP samples were obtained from donors who had a clinical diagnosis of COVID-19 and either a positive RT-PCR or SARS-CoV-2 antibody test. On the day of donation, donors were required to be healthy and asymptomatic for at least 4 weeks. The date of collection ranged from 4 to 10 weeks after symptom resolution.

SARS-CoV-2 Pseudotyped Lentivirus Production and Viral Neutralization Assays. SARS-CoV-2 spike-pseudotyped lentivirus was produced in HEK293T cells via calcium phosphate transfection. Six million cells were seeded in D10 medium (DMEM + additives: 10% fetal bovine serum, L-glutamate, penicillin, streptomycin, and 10 mM HEPES) in 10 cm plates 1 day prior to transfection. A five-plasmid system[47] was used for viral production: the lentiviral packaging vector (pHAGE_Luc2_IRES_ZsGreen), the SARS-CoV-2 spike, and lentiviral helper plasmids (HDM-Hgpm2, HDM-Tat1b, and pRC-CMV_Rev1b). The spike vector contained the full-length wild-type spike sequence from the Wuhan-Hu-1 strain of SARS-CoV-2 (GenBank NC_045512). Plasmids were added to filter-sterilized water as follows: 10 μg of pHAGE_Luc2_IRS_ZsGreen, 3.4 μg of SARS-CoV-2 spike, 2.2 μg of HDM-Hgpm2, 2.2 μg of HDM-Tat1b, and 2.2 μg of pRC-CMV_Rev1b in a final volume of 500 μL. HEPES-buffered Saline (2×, pH 7.0) was added dropwise to this mixture to a final volume of 1 mL. To form transfection complexes, 100 μL of 2.5 M $CaCl_2$ was added dropwise while the solution was gently agitated. Transfection reactions were incubated for 20 min at room temperature and then added dropwise to plated cells. Medium was removed ∼24 h post-transfection and replaced with fresh D10 medium. Virus-containing culture supernatants were harvested ∼72 h post-transfection via centrifugation at 300*g* for 5 min and filtered through a 0.45 μm filter. Viral stocks were aliquoted and stored at −80 °C until use.

For viral neutralization assays, ACE2/HeLa[48] cells were plated in white-walled clear-bottom 96-well plates at 5000 cells/well 1 day prior to infection or at 2500 cells/well 2 days prior to infection. Mouse serum was centrifuged at 2000*g* for 15 min, heat inactivated for 30 min at 56 °C, and diluted in D10 medium. Virus was diluted in D10 medium, supplemented with Polybrene, and then added to inhibitor dilutions. Polybrene was present at a final concentration of 5 μg/mL in diluted samples. Purified mAbs were filtered through a 0.22 μm filter prior to neutralization assays. Virus/inhibitor dilutions were incubated at 37 °C for 1 h. After incubation, medium was removed from cells, replaced with an equivalent volume of inhibitor/virus dilutions, and incubated at 37 °C for ∼48 h. Cells were lysed by adding BriteLite assay readout solution (PerkinElmer), and luminescence values were measured with a BioTek plate reader. Each plate was normalized by averaging RLUs from wells with cells only (0% infectivity) and virus only

https://dx.doi.org/10.1021/acscentsci.0c01405
ACS Cent. Sci. 2021, 7, 183−199

(100% infectivity). Normalized values were fitted with a three-parameter nonlinear regression inhibitor curve in GraphPad Prism 8.4.1 to obtain IC_{50} values. Fits for all serum neutralization assays were constrained to have a value of 0% at the bottom of the fit. The limit of quantitation for this assay is approximately 1:100 serum dilution. Serum samples that failed to neutralize or that neutralized at levels higher than 1:100 were set at the limit of quantitation for statistical analyses. Plots in Figure 4B−E are shown starting at the reciprocal serum dilution of the limit of quantitation (10^2).

Statistical Analyses. All normalization, cure-fitting, and statistical analysis described below were performed using GraphPad Prism 8.4.1.

For ELISA, binding titers of RBD and spike were determined for each mouse by performing 8-point serial serum dilutions started at 1:50 with 10-fold dilutions in duplicate, with replicates performed on separate days. Background subtracted replicates for each mouse were compiled and fitted with a three-parameter nonlinear regression activation curve to obtain an EC_{50} value for each serum binding from each animal to each antigen. Data were then compiled per group for each time point. Statistical comparisons between groups were performed using a Kruskal−Wallis ANOVA followed by Dunn's multiple comparisons test. Significance for comparisons between groups is indicated in Figure 4B,D: * = $p \leq 0.05$, ** = $p \leq 0.01$, *** = $p \leq 0.001$, **** = $p \leq 0.0001$. Compiled data from Dunn's multiple comparisons tests between groups for ELISA titers can be found in Table S2.

For lentiviral neutralization assays, serum from each animal at each time point was assessed in duplicate with a 6-point serial dilution (starting at 1:50 with 5-fold dilutions). Each assay was performed again in a separate experimental replicate. Each dilution series was normalized to 0% and 100% infectivity using the average RLU values of wells with cells only and with virus only, respectively, from each plate. Four normalized curves for each animal at each time point were compiled to obtain an IC_{50} value. Statistical comparisons between groups were performed using a Kruskal−Wallis ANOVA followed by Dunn's multiple comparisons test. Significance for comparisons between groups is indicated in Figure 4C,E: * = $p \leq 0.05$, ** = $p \leq 0.01$, *** = $p \leq 0.001$, **** = $p \leq 0.0001$. Compiled data from Dunn's multiple comparisons tests between groups for neutralization titers can be found in Table S3.

Safety Statement. No unexpected or unusually high safety hazards were encountered.

Data Availability. The cryo-EM map of the SΔC-Fer nanoparticle has been deposited in the wwPDB OneDep System under EMD accession code EMD-23220.

■ ASSOCIATED CONTENT

Supporting Information

The Supporting Information is available free of charge at https://pubs.acs.org/doi/10.1021/acscentsci.0c01405.

Additional data and figures including expression levels, size-exclusion chromatography, cryo-EM, ELISA results, assay validation, and off-target antibody responses (PDF)

■ AUTHOR INFORMATION

Corresponding Author

Peter S. Kim − *Department of Biochemistry & Stanford ChEM-H, Stanford University, Stanford, California 94305, United States; Chan Zuckerberg Biohub, San Francisco, California 94158, United States;* orcid.org/0000-0001-6503-4541; Email: kimpeter@stanford.edu

Authors

Abigail E. Powell − *Department of Biochemistry & Stanford ChEM-H, Stanford University, Stanford, California 94305, United States;* orcid.org/0000-0001-6408-9495

Kaiming Zhang − *Department of Bioengineering & James H. Clark Center, Stanford University, Stanford, California 94305, United States;* orcid.org/0000-0003-0414-4776

Mrinmoy Sanyal − *Department of Biochemistry & Stanford ChEM-H, Stanford University, Stanford, California 94305, United States*

Shaogeng Tang − *Department of Biochemistry & Stanford ChEM-H, Stanford University, Stanford, California 94305, United States*

Payton A. Weidenbacher − *Department of Biochemistry & Stanford ChEM-H and Department of Chemistry, Stanford University, Stanford, California 94305, United States*

Shanshan Li − *Department of Bioengineering & James H. Clark Center, Stanford University, Stanford, California 94305, United States*

Tho D. Pham − *Department of Pathology, Stanford University, Stanford, California 94305, United States; Stanford Blood Center, Palo Alto, California 94304, United States*

John E. Pak − *Chan Zuckerberg Biohub, San Francisco, California 94158, United States*

Wah Chiu − *Department of Bioengineering & James H. Clark Center, Stanford University, Stanford, California 94305, United States; Chan Zuckerberg Biohub, San Francisco, California 94158, United States; Division of CryoEM and Bioimaging, SSRL, SLAC National Accelerator Laboratory, Menlo Park, California 94025, United States;* orcid.org/0000-0002-8910-3078

Complete contact information is available at: https://pubs.acs.org/10.1021/acscentsci.0c01405

Author Contributions

A.E.P., P.A.W., S.T., M.S., and P.S.K. designed experiments. A.E.P. and S.T. purified antigens for immunization. M.S. performed mouse work. P.A.W. performed protein quantitation experiments and analysis. A.E.P. performed antigen characterization, serum ELISAs and neutralizations, and data analysis. K.Z. performed cryo-EM sample preparation, data collection, and image processing. S.L. assisted with image processing. K.Z., S.L., and W.C. analyzed the cryo-EM data. T.D.P. collected convalescent plasma samples. J.E.P. assisted with protein characterization methods and optimization. A.E.P. and P.S.K. wrote the manuscript. All authors assisted with editing and approved the final version of the manuscript.

Notes

The authors declare the following competing financial interest(s): A.E.P., P.A.W., and P.S.K. are named as inventors on a provisional patent application applied for by Stanford University and the Chan Zuckerberg Biohub on immunogenic coronavirus fusion proteins and related methods.

https://dx.doi.org/10.1021/acscentsci.0c01405
ACS Cent. Sci. 2021, 7, 183−199

■ ACKNOWLEDGMENTS

We thank Dr. Jesse Bloom, Kate Crawford, Dr. Dennis Burton, and Dr. Deli Huang for sharing the plasmids, cells, and invaluable advice for implementation of the spike-pseudotyped lentiviral neutralization assay. We thank Dr. Florian Krammer and Fatima Amanat for providing the SARS-CoV-2 RBD and FL 2P spike plasmids for protein production. We thank Nielson Weng and Dr. Nicholas Tierney for advice on statistical analyses. We thank Dr. Duo Xu for designing and providing the structural representations of spike and ferritin in Figure 1. We thank Dr. Corey Liu and the Stanford ChEM-H Macromolecular Knowledge Center for kindly relocating the GE Amersham 600 imager to our lab space during the pandemic shutdown for us to rapidly begin this work. We thank Drs. Corey Hecksel and Patrick Mitchell for expert maintenance of Stanford-SLAC Cryo-EM Center and the SLAC National Accelerator Laboratory for supporting these studies during the pandemic shutdown. We thank members of the Kim Lab for fruitful discussions and insight on project design as well as helpful comments on the manuscript. We acknowledge BioRender for the images used in Figure 2A. The CMV/R expression vectors were received from the NIH AIDS Reagent Program. This work was supported by the Stanford Maternal and Child Health Research Institute postdoctoral fellowship (to A.E.P.), the Damon Runyon Cancer Research Foundation Merck Fellowship (DRG-2301-17 to S.T.), National Institutes of Health grants (P41GM103832, R01AI148382, P01AI120943, S10OD02160 to W.C.), Chan Zuckerberg Biohub (to W.C. and P.S.K.), the Virginia and D. K. Ludwig Fund for Cancer Research (to P.S.K.), and the Frank Quattrone and Denise Foderaro Family Research Fund (to P.S.K.).

■ REFERENCES

(1) World Health Organization. *WHO Coronavirus Disease (COVID-19) Dashboard*. https://covid19.who.int/ (accessed 02 December 2020).

(2) Xia, S.; Liu, M.; Wang, C.; Xu, W.; Lan, Q.; Feng, S.; Qi, F.; Bao, L.; Du, L.; Liu, S.; Qin, C.; Sun, F.; Shi, Z.; Zhu, Y.; Jiang, S.; Lu, L. Inhibition of SARS-CoV-2 (Previously 2019-NCoV) Infection by a Highly Potent Pan-Coronavirus Fusion Inhibitor Targeting Its Spike Protein That Harbors a High Capacity to Mediate Membrane Fusion. *Cell Res.* **2020**, *30* (4), 343−355.

(3) Wrapp, D.; Wang, N.; Corbett, K. S.; Goldsmith, J. A.; Hsieh, C. L.; Abiona, O.; Graham, B. S.; McLellan, J. S. Cryo-EM Structure of the 2019-NCoV Spike in the Prefusion Conformation. *Science* **2020**, *367* (6483), 1260−1263.

(4) Robbiani, D. F.; Gaebler, C.; Muecksch, F.; Lorenzi, J. C. C.; Wang, Z.; Cho, A.; Agudelo, M.; Barnes, C. O.; Gazumyan, A.; Finkin, S.; Hägglöf, T.; Oliveira, T. Y.; Viant, C.; Hurley, A.; Hoffmann, H.-H.; Millard, K. G.; Kost, R. G.; Cipolla, M.; Gordon, K.; Bianchini, F.; Chen, S. T.; Ramos, V.; Patel, R.; Dizon, J.; Shimeliovich, I.; Mendoza, P.; Hartweger, H.; Nogueira, L.; Pack, M.; Horowitz, J.; Schmidt, F.; Weisblum, Y.; Michailidis, E.; Ashbrook, A. W.; Waltari, E.; Pak, J. E.; Huey-Tubman, K. E.; Koranda, N.; Hoffman, P. R.; West, A. P.; Rice, C. M.; Hatziioannou, T.; Bjorkman, P. J.; Bieniasz, P. D.; Caskey, M.; Nussenzweig, M. C. Convergent Antibody Responses to SARS-CoV-2 in Convalescent Individuals. *Nature* **2020**, *584* (7821), 437−442.

(5) Brouwer, P. J. M.; Caniels, T. G.; van der Straten, K.; Snitselaar, J. L.; Aldon, Y.; Bangaru, S.; Torres, J. L.; Okba, N. M. A.; Claireaux, M.; Kerster, G.; Bentlage, A. E. H.; van Haaren, M. M.; Guerra, D.; Burger, J. A.; Schermer, E. E.; Verheul, K. D.; van der Velde, N.; van der Kooi, A.; van Schooten, J.; van Breemen, M. J.; Bijl, T. P. L.; Sliepen, K.; Aartse, A.; Derking, R.; Bontjer, I.; Kootstra, N. A.; Wiersinga, W. J.; Vidarsson, G.; Haagmans, B. L.; Ward, A. B.; de Bree, G. J.; Sanders, R. W.; van Gils, M. J. Potent Neutralizing Antibodies from COVID-19 Patients Define Multiple Targets of Vulnerability. *Science* **2020**, *369* (6504), 643−650.

(6) Hoffmann, M.; Kleine-Weber, H.; Pöhlmann, S. A Multibasic Cleavage Site in the Spike Protein of SARS-CoV-2 Is Essential for Infection of Human Lung Cells. *Mol. Cell* **2020**, *78* (4), 779−784.

(7) Walls, A. C.; Park, Y.-J.; Tortorici, M. A.; Wall, A.; McGuire, A. T.; Veesler, D. Structure, Function, and Antigenicity of the SARS-CoV-2 Spike Glycoprotein. *Cell* **2020**, *181* (2), 281−292.

(8) Yan, R.; Zhang, Y.; Li, Y.; Xia, L.; Guo, Y.; Zhou, Q. Structural Basis for the Recognition of SARS-CoV-2 by Full-Length Human ACE2. *Science* **2020**, *367* (6485), 1444−1448.

(9) Shang, J.; Ye, G.; Shi, K.; Wan, Y.; Luo, C.; Aihara, H.; Geng, Q.; Auerbach, A.; Li, F. Structural Basis of Receptor Recognition by SARS-CoV-2. *Nature* **2020**, *581* (7807), 221−224.

(10) Lan, J.; Ge, J.; Yu, J.; Shan, S.; Zhou, H.; Fan, S.; Zhang, Q.; Shi, X.; Wang, Q.; Zhang, L.; Wang, X. Structure of the SARS-CoV-2 Spike Receptor-Binding Domain Bound to the ACE2 Receptor. *Nature* **2020**, *581* (7807), 215−220.

(11) Corbett, K. S.; Flynn, B.; Foulds, K. E.; Francica, J. R.; Boyoglu-Barnum, S.; Werner, A. P.; Flach, B.; O'Connell, S.; Bock, K. W.; Minai, M.; Nagata, B. M.; Andersen, H.; Martinez, D. R.; Noe, A. T.; Douek, N.; Donaldson, M. M.; Nji, N. N.; Alvarado, G. S.; Edwards, D. K.; Flebbe, D. R.; Lamb, E.; Doria-Rose, N. A.; Lin, B. C.; Louder, M. K.; O'Dell, S.; Schmidt, S. D.; Phung, E.; Chang, L. A.; Yap, C.; Todd, J.-P. M.; Pessaint, L.; Van Ry, A.; Browne, S.; Greenhouse, J.; Putman-Taylor, T.; Strasbaugh, A.; Campbell, T.-A.; Cook, A.; Dodson, A.; Steingrebe, K.; Shi, W.; Zhang, Y.; Abiona, O. M.; Wang, L.; Pegu, A.; Yang, E. S.; Leung, K.; Zhou, T.; Teng, I.-T.; Widge, A.; Gordon, I.; Novik, L.; Gillespie, R. A.; Loomis, R. J.; Moliva, J. I.; Stewart-Jones, G.; Himansu, S.; Kong, W.-P.; Nason, M. C.; Morabito, K. M.; Ruckwardt, T. J.; Ledgerwood, J. E.; Gaudinski, M. R.; Kwong, P. D.; Mascola, J. R.; Carfi, A.; Lewis, M. G.; Baric, R. S.; McDermott, A.; Moore, I. N.; Sullivan, N. J.; Roederer, M.; Seder, R. A.; Graham, B. S. Evaluation of the MRNA-1273 Vaccine against SARS-CoV-2 in Nonhuman Primates. *N. Engl. J. Med.* **2020**, *383*, 1544.

(12) Corbett, K. S.; Edwards, D.; Leist, S. R.; Abiona, O. M.; Boyoglu-Barnum, S.; Gillespie, R. A.; Himansu, S.; Schäfer, A.; Ziwawo, C. T.; DiPiazza, A. T.; Dinnon, K. H.; Elbashir, S. M.; Shaw, C. A.; Woods, A.; Fritch, E. J.; Martinez, D. R.; Bock, K. W.; Minai, M.; Nagata, B. M.; Hutchinson, G. B.; Bahl, K.; Garcia-Dominguez, D.; Ma, L.; Renzi, I.; Kong, W.-P.; Schmidt, S. D.; Wang, L.; Zhang, Y.; Stevens, L. J.; Phung, E.; Chang, L. A.; Loomis, R. J.; Altaras, N. E.; Narayanan, E.; Metkar, M.; Presnyak, V.; Liu, C.; Louder, M. K.; Shi, W.; Leung, K.; Yang, E. S.; West, A.; Gully, K. L.; Wang, N.; Wrapp, D.; Doria-Rose, N. A.; Stewart-Jones, G.; Bennett, H.; Nason, M. C.; Ruckwardt, T. J.; McLellan, J. S.; Denison, M. R.; Chappell, J. D.; Moore, I. N.; Morabito, K. M.; Mascola, J. R.; Baric, R. S.; Carfi, A.; Graham, B. S. SARS-CoV-2 MRNA Vaccine Development Enabled by Prototype Pathogen Preparedness. *Nature* **2020**, *586*, 567.

(13) Smith, T. R. F.; Patel, A.; Ramos, S.; Elwood, D.; Zhu, X.; Yan, J.; Gary, E. N.; Walker, S. N.; Schultheis, K.; Purwar, M.; Xu, Z.; Walters, J.; Bhojnagarwala, P.; Yang, M.; Chokkalingam, N.; Pezzoli, P.; Parzych, E.; Reuschel, E. L.; Doan, A.; Tursi, N.; Vasquez, M.; Choi, J.; Tello-Ruiz, E.; Maricic, I.; Bah, M. A.; Wu, Y.; Amante, D.; Park, D. H.; Dia, Y.; Ali, A. R.; Zaidi, F. I.; Generotti, A.; Kim, K. Y.; Herring, T. A.; Reeder, S.; Andrade, V. M.; Buttigieg, K.; Zhao, G.; Wu, J. M.; Li, D.; Bao, L.; Liu, J.; Deng, W.; Qin, C.; Brown, A. S.; Khoshnejad, M.; Wang, N.; Chu, J.; Wrapp, D.; McLellan, J. S.; Muthumani, K.; Wang, B.; Carroll, M. W.; Kim, J. J.; Boyer, J.; Kulp, D. W.; Humeau, L. M. P. F.; Weiner, D. B.; Broderick, K. E. Immunogenicity of a DNA Vaccine Candidate for COVID-19. *Nat. Commun.* **2020**, *11* (1), 1−13.

(14) Wang, H.; Zhang, Y.; Huang, B.; Deng, W.; Quan, Y.; Wang, W.; Xu, W.; Zhao, Y.; Li, N.; Zhang, J.; Liang, H.; Bao, L.; Xu, Y.; Ding, L.; Zhou, W.; Gao, H.; Liu, J.; Niu, P.; Zhao, L.; Zhen, W.; Fu, H.; Yu, S.; Zhang, Z.; Xu, G.; Li, C.; Lou, Z.; Xu, M.; Qin, C.; Wu, G.;

https://dx.doi.org/10.1021/acscentsci.0c01405
ACS Cent. Sci. 2021, 7, 183−199

Gao, G. F.; Tan, W.; Yang, X. Development of an Inactivated Vaccine Candidate, BBIBP-CorV, with Potent Protection against SARS-CoV-2. *Cell* **2020**, *182* (3), 713−721.
(15) van Doremalen, N.; Lambe, T.; Spencer, A.; Belij-Rammerstorfer, S.; Purushotham, J. N.; Port, J. R.; Avanzato, V. A.; Bushmaker, T.; Flaxman, A.; Ulaszewska, M.; Feldmann, F.; Allen, E. R.; Sharpe, H.; Schulz, J.; Holbrook, M.; Okumura, A.; Meade-White, K.; Pérez-Pérez, L.; Edwards, N. J.; Wright, D.; Bissett, C.; Gilbride, C.; Williamson, B. N.; Rosenke, R.; Long, D.; Ishwarbhai, A.; Kailath, R.; Rose, L.; Morris, S.; Powers, C.; Lovaglio, J.; Hanley, P. W.; Scott, D.; Saturday, G.; de Wit, E.; Gilbert, S. C.; Munster, V. J. ChAdOx1 NCoV-19 Vaccine Prevents SARS-CoV-2 Pneumonia in Rhesus Macaques. *Nature* **2020**, *586*, 578.
(16) Folegatti, P. M.; Ewer, K. J.; Aley, P. K.; Angus, B.; Becker, S.; Belij-Rammerstorfer, S.; Bellamy, D.; Bibi, S.; Bittaye, M.; Clutterbuck, E. A.; Dold, C.; Faust, S. N.; Finn, A.; Flaxman, A. L.; Hallis, B.; Heath, P.; Jenkin, D.; Lazarus, R.; Makinson, R.; Minassian, A. M.; Pollock, K. M.; Ramasamy, M.; Robinson, H.; Snape, M.; Tarrant, R.; Voysey, M.; Green, C.; Douglas, A. D.; Hill, A. V. S.; Lambe, T.; Gilbert, S. C.; Pollard, A. J.; Aboagye, J.; Adams, K.; Ali, A.; Allen, E.; Allison, J. L.; Anslow, R.; Arbe-Barnes, E. H.; Babbage, G.; Baillie, K.; Baker, M.; Baker, N.; Baker, P.; Baleanu, I.; Ballaminut, J.; Barnes, E.; Barrett, J.; Bates, L.; Batten, A.; Beadon, K.; Beckley, R.; Berrie, E.; Berry, L.; Beveridge, A.; Bewley, K. R.; Bijker, E. M.; Bingham, T.; Blackwell, L.; Blundell, C. L.; Bolam, E.; Boland, E.; Borthwick, N.; Bower, T.; Boyd, A.; Brenner, T.; Bright, P. D.; Brown-O'Sullivan, C.; Brunt, E.; Burbage, J.; Burge, S.; Buttigieg, K. R.; Byard, N.; Cabera Puig, I.; Calvert, A.; Camara, S.; Cao, M.; Cappuccini, F.; Carr, M.; Carroll, M. W.; Carter, V.; Cathie, K.; Challis, R. J.; Charlton, S.; Chelysheva, I.; Cho, J.-S.; Cicconi, P.; Cifuentes, L.; Clark, H.; Clark, E.; Cole, T.; Colin-Jones, R.; Conlon, C. P.; Cook, A.; Coombes, N. S.; Cooper, R.; Cosgrove, C. A.; Coy, K.; Crocker, W. E. M.; Cunningham, C. J.; Damratoski, B. E.; Dando, L.; Datoo, M. S.; Davies, H.; De Graaf, H.; Demissie, T.; Di Maso, C.; Dietrich, I.; Dong, T.; Donnellan, F. R.; Douglas, N.; Downing, C.; Drake, J.; Drake-Brockman, R.; Drury, R. E.; Dunachie, S. J.; Edwards, N. J.; Edwards, F. D. L.; Edwards, C. J.; Elias, S. C.; Elmore, M. J.; Emary, K. R. W.; English, M. R.; Fagerbrink, S.; Felle, S.; Feng, S.; Field, S.; Fixmer, C.; Fletcher, C.; Ford, K. J.; Fowler, J.; Fox, P.; Francis, E.; Frater, J.; Furze, J.; Fuskova, M.; Galiza, E.; Gbesemete, D.; Gilbride, C.; Godwin, K.; Gorini, G.; Goulston, L.; Grabau, C.; Gracie, L.; Gray, Z.; Guthrie, L. B.; Hackett, M.; Halwe, S.; Hamilton, E.; Hamlyn, J.; Hanumunthadu, B.; Harding, I.; Harris, S. A.; Harris, A.; Harrison, D.; Harrison, C.; Hart, T. C.; Haskell, L.; Hawkins, S.; Head, I.; Henry, J. A.; Hill, J.; Hodgson, S. H. C.; Hou, M. M.; Howe, E.; Howell, N.; Hutlin, C.; Ikram, S.; Isitt, C.; Iveson, P.; Jackson, S.; Jackson, F.; James, S. W.; Jenkins, M.; Jones, E.; Jones, K.; Jones, C. E.; Jones, B.; Kailath, R.; Karampatsas, K.; Keen, J.; Kelly, S.; Kelly, D.; Kerr, D.; Kerridge, S.; Khan, L.; Khan, U.; Killen, A.; Kinch, J.; King, T. B.; King, L.; King, J.; Kingham-Page, L.; Klenerman, P.; Knapper, F.; Knight, J. C.; Knott, D.; Koleva, S.; Kupke, A.; Larkworthy, C. W.; Larwood, J. P. J.; Laskey, A.; Lawrie, A. M.; Lee, A.; Ngan Lee, K. Y.; Lees, E. A.; Legge, H.; Lelliott, A.; Lemm, N.-M.; Lias, A. M.; Linder, A.; Lipworth, S.; Liu, X.; Liu, S.; Lopez Ramon, R.; Lwin, M.; Mabesa, F.; Madhavan, M.; Mallett, G.; Mansatta, K.; Marcal, I.; Marinou, S.; Marlow, E.; Marshall, J. L.; Martin, J.; McEwan, J.; McInroy, L.; Meddaugh, G.; Mentzer, A. J.; Mirtorabi, N.; Moore, M.; Moran, E.; Morey, E.; Morgan, V.; Morris, S. J.; Morrison, H.; Morshead, G.; Morter, R.; Mujadidi, Y. F.; Muller, J.; Munera-Huertas, T.; Munro, C.; Munro, A.; Murphy, S.; Munster, V. J.; Mweu, P.; Noé, A.; Nugent, F. L.; Nuthall, E.; O'Brien, K.; O'Connor, D.; Oguti, B.; Oliver, J. L.; Oliveira, C.; O'Reilly, P. J.; Osborn, M.; Osborne, P.; Owen, C.; Owens, D.; Owino, N.; Pacurar, M.; Parker, K.; Parracho, H.; Patrick-Smith, M.; Payne, V.; Pearce, J.; Peng, Y.; Peralta Alvarez, M. P.; Perring, J.; Pfafferott, K.; Pipini, D.; Plested, E.; Pluess-Hall, H.; Pollock, K.; Poulton, I.; Presland, L.; Provstgaard-Morys, S.; Pulido, D.; Radia, K.; Ramos Lopez, F.; Rand, J.; Ratcliffe, H.; Rawlinson, T.; Rhead, S.; Riddell, A.; Ritchie, A. J.; Roberts, H.; Robson, J.; Roche, S.; Rohde, C.; Rollier, C. S.; Romani, R.; Rudiansyah, I.; Saich, S.; Sajjad, S.; Salvador, S.; Sanchez Riera, L.; Sanders, H.; Sanders, K.; Sapaun, S.; Sayce, C.; Schofield, E.; Screaton, G.; Selby, B.; Semple, C.; Sharpe, H. R.; Shaik, I.; Shea, A.; Shelton, H.; Silk, S.; Silva-Reyes, L.; Skelly, D. T.; Smee, H.; Smith, C. C.; Smith, D. J.; Song, R.; Spencer, A. J.; Stafford, E.; Steele, A.; Stefanova, E.; Stockdale, L.; Szigeti, A.; Tahiri-Alaoui, A.; Tait, M.; Talbot, H.; Tanner, R.; Taylor, I. J.; Taylor, V.; Te Water Naude, R.; Thakur, N.; Themistocleous, Y.; Themistocleous, A.; Thomas, M.; Thomas, T. M.; Thompson, A.; Thomson-Hill, S.; Tomlins, J.; Tonks, S.; Towner, J.; Tran, N.; Tree, J. A.; Truby, A.; Turkentine, K.; Turner, C.; Turner, N.; Turner, S.; Tuthill, T.; Ulaszewska, M.; Varughese, R.; Van Doremalen, N.; Veighey, K.; Verheul, M. K.; Vichos, I.; Vitale, E.; Walker, L.; Watson, M. E. E.; Welham, B.; Wheat, J.; White, C.; White, R.; Worth, A. T.; Wright, D.; Wright, S.; Yao, X. L.; Yau, Y. Safety and Immunogenicity of the ChAdOx1 NCoV-19 Vaccine against SARS-CoV-2: A Preliminary Report of a Phase 1/2, Single-Blind, Randomised Controlled Trial. *Lancet* **2020**, *396* (10249), 467−478.
(17) Gao, Q.; Bao, L.; Mao, H.; Wang, L.; Xu, K.; Yang, M.; Li, Y.; Zhu, L.; Wang, N.; Lv, Z.; Gao, H.; Ge, X.; Kan, B.; Hu, Y.; Liu, J.; Cai, F.; Jiang, D.; Yin, Y.; Qin, C.; Li, J.; Gong, X.; Lou, X.; Shi, W.; Wu, D.; Zhang, H.; Zhu, L.; Deng, W.; Li, Y.; Lu, J.; Li, C.; Wang, X.; Yin, W.; Zhang, Y.; Qin, C. Development of an Inactivated Vaccine Candidate for SARS-CoV-2. *Science* **2020**, *369* (6499), 77−81.
(18) Graham, S. P.; McLean, R. K.; Spencer, A. J.; Belij-Rammerstorfer, S.; Wright, D.; Ulaszewska, M.; Edwards, J. C.; Hayes, J. W. P.; Martini, V.; Thakur, N.; Conceicao, C.; Dietrich, I.; Shelton, H.; Waters, R.; Ludi, A.; Wilsden, G.; Browning, C.; Bialy, D.; Bhat, S.; Stevenson-Leggett, P.; Hollinghurst, P.; Gilbride, C.; Pulido, D.; Moffat, K.; Sharpe, H.; Allen, E.; Mioulet, V.; Chiu, C.; Newman, J.; Asfor, A. S.; Burman, A.; Crossley, S.; Huo, J.; Owens, R. J.; Carroll, M.; Hammond, J. A.; Tchilian, E.; Bailey, D.; Charleston, B.; Gilbert, S. C.; Tuthill, T. J.; Lambe, T. Evaluation of the Immunogenicity of Prime-Boost Vaccination with the Replication-Deficient Viral Vectored COVID-19 Vaccine Candidate ChAdOx1 NCoV-19. *npj Vaccines* **2020**, *5* (1), 69.
(19) Walsh, E. E.; Frenck, R. W.; Falsey, A. R.; Kitchin, N.; Absalon, J.; Gurtman, A.; Lockhart, S.; Neuzil, K.; Mulligan, M. J.; Bailey, R.; Swanson, K. A.; Li, P.; Koury, K.; Kalina, W.; Cooper, D.; Fontes-Garfias, C.; Shi, P.-Y.; Türeci, Ö.; Tompkins, K. R.; Lyke, K. E.; Raabe, V.; Dormitzer, P. R.; Jansen, K. U.; Şahin, U.; Gruber, W. C. Safety and Immunogenicity of Two RNA-Based Covid-19 Vaccine Candidates. *N. Engl. J. Med.* **2020**, *383*, 2439.
(20) Funk, C. D.; Laferrière, C.; Ardakani, A. A Snapshot of the Global Race for Vaccines Targeting SARS-CoV-2 and the COVID-19 Pandemic. *Front. Pharmacol.* **2020**, *11*, 11.
(21) Krammer, F. SARS-CoV-2 Vaccines in Development. *Nature* **2020**, *586* (7830), 516−527.
(22) Thanh Le, T.; Andreadakis, Z.; Kumar, A.; Gómez Román, R.; Tollefsen, S.; Saville, M.; Mayhew, S. The COVID-19 Vaccine Development Landscape. *Nat. Rev. Drug Discovery* **2020**, *19* (5), 305−306.
(23) Fausther-Bovendo, H.; Kobinger, G. P. Pre-Existing Immunity against Ad Vectors. *Hum. Vaccines Immunother.* **2014**, *10* (10), 2875−2884.
(24) Thacker, E. E.; Timares, L.; Matthews, Q. L. Strategies to Overcome Host Immunity to Adenovirus Vectors in Vaccine Development. *Expert Rev. Vaccines* **2009**, *8* (6), 761−777.
(25) Moyle, P. M.; Toth, I. Modern Subunit Vaccines: Development, Components, and Research Opportunities. *ChemMedChem* **2013**, *8* (3), 360−376.
(26) Wang, N.; Shang, J.; Jiang, S.; Du, L. Subunit Vaccines Against Emerging Pathogenic Human Coronaviruses. *Front. Microbiol.* **2020**, *11*, 11.
(27) Chattopadhyay, S.; Chen, J.-Y.; Chen, H.-W.; Hu, C.-M. J. Nanoparticle Vaccines Adopting Virus-like Features for Enhanced Immune Potentiation. *Nanotheranostics* **2017**, *1* (3), 244−260.

(28) López-Sagaseta, J.; Malito, E.; Rappuoli, R.; Bottomley, M. J. Self-Assembling Protein Nanoparticles in the Design of Vaccines. *Comput. Struct. Biotechnol. J.* **2016**, *14*, 58−68.
(29) Zhao, L.; Seth, A.; Wibowo, N.; Zhao, C.-X.; Mitter, N.; Yu, C.; Middelberg, A. P. J. Nanoparticle Vaccines. *Vaccine* **2014**, *32* (3), 327−337.
(30) Kanekiyo, M.; Bu, W.; Joyce, M. G.; Meng, G.; Whittle, J. R. R.; Baxa, U.; Yamamoto, T.; Narpala, S.; Todd, J.-P.; Rao, S. S.; McDermott, A. B.; Koup, R. A.; Rossmann, M. G.; Mascola, J. R.; Graham, B. S.; Cohen, J. I.; Nabel, G. J. Rational Design of an Epstein-Barr Virus Vaccine Targeting the Receptor-Binding Site. *Cell* **2015**, *162* (5), 1090−1100.
(31) Walls, A. C.; Fiala, B.; Schäfer, A.; Wrenn, S.; Pham, M. N.; Murphy, M.; Tse, L. V.; Shehata, L.; O'Connor, M. A.; Chen, C.; Navarro, M. J.; Miranda, M. C.; Pettie, D.; Ravichandran, R.; Kraft, J. C.; Ogohara, C.; Palser, A.; Chalk, S.; Lee, E. C.; Guerriero, K.; Kepl, E.; Chow, C. M.; Sydeman, C.; Hodge, E. A.; Brown, B.; Fuller, J. T.; Dinnon, K. H.; Gralinski, L. E.; Leist, S. R.; Gully, K. L.; Lewis, T. B.; Guttman, M.; Chu, H. Y.; Lee, K. K.; Fuller, D. H.; Baric, R. S.; Kellam, P.; Carter, L.; Pepper, M.; Sheahan, T. P.; Veesler, D.; King, N. P. Elicitation of Potent Neutralizing Antibody Responses by Designed Protein Nanoparticle Vaccines for SARS-CoV-2. *Cell* **2020**, *183*, 1367.
(32) Zhang, B.; Chao, C. W.; Tsybovsky, Y.; Abiona, O. M.; Hutchinson, G. B.; Moliva, J. I.; Olia, A. S.; Pegu, A.; Phung, E.; Stewart-Jones, G. B. E.; Verardi, R.; Wang, L.; Wang, S.; Werner, A.; Yang, E. S.; Yap, C.; Zhou, T.; Mascola, J. R.; Sullivan, N. J.; Graham, B. S.; Corbett, K. S.; Kwong, P. D. A Platform Incorporating Trimeric Antigens into Self-Assembling Nanoparticles Reveals SARS-CoV-2-Spike Nanoparticles to Elicit Substantially Higher Neutralizing Responses than Spike Alone. *Sci. Rep.* **2020**, in press. DOI: 10.1038/s41598-020-74949-2.
(33) Kanekiyo, M.; Wei, C.-J.; Yassine, H. M.; McTamney, P. M.; Boyington, J. C.; Whittle, J. R. R.; Rao, S. S.; Kong, W.-P.; Wang, L.; Nabel, G. J. Self-Assembling Influenza Nanoparticle Vaccines Elicit Broadly Neutralizing H1N1 Antibodies. *Nature* **2013**, *499* (7456), 102−106.
(34) Yassine, H. M.; Boyington, J. C.; McTamney, P. M.; Wei, C.-J.; Kanekiyo, M.; Kong, W.-P.; Gallagher, J. R.; Wang, L.; Zhang, Y.; Joyce, M. G.; Lingwood, D.; Moin, S. M.; Andersen, H.; Okuno, Y.; Rao, S. S.; Harris, A. K.; Kwong, P. D.; Mascola, J. R.; Nabel, G. J.; Graham, B. S. Hemagglutinin-Stem Nanoparticles Generate Heterosubtypic Influenza Protection. *Nat. Med.* **2015**, *21* (9), 1065−1070.
(35) Sliepen, K.; Ozorowski, G.; Burger, J. A.; van Montfort, T.; Stunnenberg, M.; LaBranche, C.; Montefiori, D. C.; Moore, J. P.; Ward, A. B.; Sanders, R. W. Presenting Native-like HIV-1 Envelope Trimers on Ferritin Nanoparticles Improves Their Immunogenicity. *Retrovirology* **2015**, *12* (1), 82.
(36) He, L.; de Val, N.; Morris, C. D.; Vora, N.; Thinnes, T. C.; Kong, L.; Azadnia, P.; Sok, D.; Zhou, B.; Burton, D. R.; Wilson, I. A.; Nemazee, D.; Ward, A. B.; Zhu, J. Presenting Native-like Trimeric HIV-1 Antigens with Self-Assembling Nanoparticles. *Nat. Commun.* **2016**, *7* (1), 12041.
(37) Kamp, H. D.; Swanson, K. A.; Wei, R. R.; Dhal, P. K.; Dharanipragada, R.; Kern, A.; Sharma, B.; Sima, R.; Hajdusek, O.; Hu, L. T.; Wei, C.-J.; Nabel, G. J. Design of a Broadly Reactive Lyme Disease Vaccine. *npj Vaccines* **2020**, *5* (1), 33.
(38) Swanson, K. A.; Rainho-Tomko, J. N.; Williams, Z. P.; Lanza, L.; Peredelchuk, M.; Kishko, M.; Pavot, V.; Alamares-Sapuay, J.; Adhikarla, H.; Gupta, S.; Chivukula, S.; Gallichan, S.; Zhang, L.; Jackson, N.; Yoon, H.; Edwards, D.; Wei, C.-J.; Nabel, G. J. A Respiratory Syncytial Virus (RSV) F Protein Nanoparticle Vaccine Focuses Antibody Responses to a Conserved Neutralization Domain. *Sci. Immunol.* **2020**, *5* (47), No. eaba6466.
(39) Cho, K. J.; Shin, H. J.; Lee, J.-H.; Kim, K.-J.; Park, S. S.; Lee, Y.; Lee, C.; Park, S. S.; Kim, K. H. The Crystal Structure of Ferritin from Helicobacter Pylori Reveals Unusual Conformational Changes for Iron Uptake. *J. Mol. Biol.* **2009**, *390* (1), 83−98.
(40) Biswas, P.; Trozado, C.; Lee, J.; Schwartz, R. M. Development of a Mammalian Cell Culture Process for Rapid Clinical-Scale Production of Novel Influenza Nanoparticle Vaccines. *BMC Proc.* **2015**, *9* (S9), O12.
(41) Ke, Z.; Oton, J.; Qu, K.; Cortese, M.; Zila, V.; McKeane, L.; Nakane, T.; Zivanov, J.; Neufeldt, C. J.; Cerikan, B.; Lu, J. M.; Peukes, J.; Xiong, X.; Kräusslich, H.-G.; Scheres, S. H. W.; Bartenschlager, R.; Briggs, J. A. G. Structures and Distributions of SARS-CoV-2 Spike Proteins on Intact Virions. *Nature* **2020**, *588*, 498.
(42) Turoňová, B.; Sikora, M.; Schürmann, C.; Hagen, W. J. H.; Welsch, S.; Blanc, F. E. C.; von Bülow, S.; Gecht, M.; Bagola, K.; Hörner, C.; van Zandbergen, G.; Landry, J.; de Azevedo, N. T. D.; Mosalaganti, S.; Schwarz, A.; Covino, R.; Mühlebach, M. D.; Hummer, G.; Krijnse Locker, J.; Beck, M. In Situ Structural Analysis of SARS-CoV-2 Spike Reveals Flexibility Mediated by Three Hinges. *Science* **2020**, *370*, No. 203.
(43) Klein, S.; Cortese, M.; Winter, S. L.; Wachsmuth-Melm, M.; Neufeldt, C. J.; Cerikan, B.; Stanifer, M. L.; Boulant, S.; Bartenschlager, R.; Chlanda, P. SARS-CoV-2 Structure and Replication Characterized by in Situ Cryo-Electron Tomography. *Nat. Commun.* **2020**, 5885.
(44) Zamecnik, C. R.; Rajan, J. V.; Yamauchi, K. A.; Mann, S. A.; Loudermilk, R. P.; Sowa, G. M.; Zorn, K. C.; Alvarenga, B. D.; Gaebler, C.; Caskey, M.; Stone, M.; Norris, P. J.; Gu, W.; Chiu, C. Y.; Ng, D.; Byrnes, J. R.; Zhou, X. X.; Wells, J. A.; Robbiani, D. F.; Nussenzweig, M. C.; DeRisi, J. L.; Wilson, M. R. ReScan, a Multiplex Diagnostic Pipeline, Pans Human Sera for SARS-CoV-2 Antigens. *Cell Reports Med.* 2020, in press. DOI: 10.1016/j.xcrm.2020.100123.
(45) Li, Y.; Ma, M.; Lei, Q.; Wang, F.; Sun, Z.; Fan, X.; Tao, S. Linear Epitope Landscape of SARS-CoV-2 Spike Protein Constructed from 1,051 COVID-19 Patients. *medRxiv* 2020. DOI: 10.1101/2020.07.13.20152587.
(46) Eckert, D. M.; Malashkevich, V. N.; Kim, P. S. Crystal Structure of GCN4-PIQI, a Trimeric Coiled Coil with Buried Polar Residues. *J. Mol. Biol.* **1998**, *284* (4), 859−865.
(47) Crawford, K. H. D.; Eguia, R.; Dingens, A. S.; Loes, A. N.; Malone, K. D.; Wolf, C. R.; Chu, H. Y.; Tortorici, M. A.; Veesler, D.; Murphy, M.; Pettie, D.; King, N. P.; Balazs, A. B.; Bloom, J. D. Protocol and Reagents for Pseudotyping Lentiviral Particles with SARS-CoV-2 Spike Protein for Neutralization Assays. *Viruses* **2020**, *12* (5), 513.
(48) Rogers, T. F.; Zhao, F.; Huang, D.; Beutler, N.; Burns, A.; He, W.; Limbo, O.; Smith, C.; Song, G.; Woehl, J.; Yang, L.; Abbott, R. K.; Callaghan, S.; Garcia, E.; Hurtado, J.; Parren, M.; Peng, L.; Ramirez, S.; Ricketts, J.; Ricciardi, M. J.; Rawlings, S. A.; Wu, N. C.; Yuan, M.; Smith, D. M.; Nemazee, D.; Teijaro, J. R.; Voss, J. E.; Wilson, I. A.; Andrabi, R.; Briney, B.; Landais, E.; Sok, D.; Jardine, J. G.; Burton, D. R. Isolation of Potent SARS-CoV-2 Neutralizing Antibodies and Protection from Disease in a Small Animal Model. *Science* **2020**, *369*, No. 956.
(49) Amanat, F.; Stadlbauer, D.; Strohmeier, S.; Nguyen, T. H. O.; Chromikova, V.; McMahon, M.; Jiang, K.; Arunkumar, G. A.; Jurczyszak, D.; Polanco, J.; Bermudez-Gonzalez, M.; Kleiner, G.; Aydillo, T.; Miorin, L.; Fierer, D. S.; Lugo, L. A.; Kojic, E. M.; Stoever, J.; Liu, S. T. H.; Cunningham-Rundles, C.; Felgner, P. L.; Moran, T.; García-Sastre, A.; Caplivski, D.; Cheng, A. C.; Kedzierska, K.; Vapalahti, O.; Hepojoki, J. M.; Simon, V.; Krammer, F. A Serological Assay to Detect SARS-CoV-2 Seroconversion in Humans. *Nat. Med.* **2020**, *26* (7), 1033−1036.
(50) Pallesen, J.; Wang, N.; Corbett, K. S.; Wrapp, D.; Kirchdoerfer, R. N.; Turner, H. L.; Cottrell, C. A.; Becker, M. M.; Wang, L.; Shi, W.; Kong, W.-P.; Andres, E. L.; Kettenbach, A. N.; Denison, M. R.; Chappell, J. D.; Graham, B. S.; Ward, A. B.; McLellan, J. S. Immunogenicity and Structures of a Rationally Designed Prefusion MERS-CoV Spike Antigen. *Proc. Natl. Acad. Sci. U. S. A.* **2017**, *114* (35), E7348−E7357.
(51) Kirchdoerfer, R. N.; Cottrell, C. A.; Wang, N.; Pallesen, J.; Yassine, H. M.; Turner, H. L.; Corbett, K. S.; Graham, B. S.;

McLellan, J. S.; Ward, A. B. Pre-Fusion Structure of a Human Coronavirus Spike Protein. *Nature* **2016**, *531* (7592), 118−121.
(52) Chen, W.-H.; Hotez, P. J.; Bottazzi, M. E. Potential for Developing a SARS-CoV Receptor-Binding Domain (RBD) Recombinant Protein as a Heterologous Human Vaccine against Coronavirus Infectious Disease (COVID)-19. *Hum. Vaccines Immunother.* **2020**, *16* (6), 1239−1242.
(53) Mulligan, M. J.; Lyke, K. E.; Kitchin, N.; Absalon, J.; Gurtman, A.; Lockhart, S.; Neuzil, K.; Raabe, V.; Bailey, R.; Swanson, K. A.; Li, P.; Koury, K.; Kalina, W.; Cooper, D.; Fontes-Garfias, C.; Shi, P.-Y.; Türeci, Ö.; Tompkins, K. R.; Walsh, E. E.; Frenck, R.; Falsey, A. R.; Dormitzer, P. R.; Gruber, W. C.; Şahin, U.; Jansen, K. U. Phase I/II Study of COVID-19 RNA Vaccine BNT162b1 in Adults. *Nature* **2020**, *586* (7830), 589−593.
(54) Watanabe, Y.; Allen, J. D.; Wrapp, D.; McLellan, J. S.; Crispin, M. Site-Specific Glycan Analysis of the SARS-CoV-2 Spike. *Science* **2020**, No. eabb9983.
(55) Yuan, M.; Wu, N. C.; Zhu, X.; Lee, C. C. D.; So, R. T. Y.; Lv, H.; Mok, C. K. P.; Wilson, I. A. A Highly Conserved Cryptic Epitope in the Receptor Binding Domains of SARS-CoV-2 and SARS-CoV. *Science* **2020**, *368* (6491), 630−633.
(56) Tian, X.; Li, C.; Huang, A.; Xia, S.; Lu, S.; Shi, Z.; Lu, L.; Jiang, S.; Yang, Z.; Wu, Y.; Ying, T. Potent Binding of 2019 Novel Coronavirus Spike Protein by a SARS Coronavirus-Specific Human Monoclonal Antibody. *Emerging Microbes Infect.* **2020**, *9* (1), 382−385.
(57) ter Meulen, J.; van den Brink, E. N.; Poon, L. L. M.; Marissen, W. E.; Leung, C. S. W.; Cox, F.; Cheung, C. Y.; Bakker, A. Q.; Bogaards, J. A.; van Deventer, E.; Preiser, W.; Doerr, H. W.; Chow, V. T.; de Kruif, J.; Peiris, J. S. M.; Goudsmit, J. Human Monoclonal Antibody Combination against SARS Coronavirus: Synergy and Coverage of Escape Mutants. *PLoS Med.* **2006**, *3* (7), No. e237.
(58) Shi, R.; Shan, C.; Duan, X.; Chen, Z.; Liu, P.; Song, J.; Song, T.; Bi, X.; Han, C.; Wu, L.; Gao, G.; Hu, X.; Zhang, Y.; Tong, Z.; Huang, W.; Liu, W. J.; Wu, G.; Zhang, B.; Wang, L.; Qi, J.; Feng, H.; Wang, F.-S.; Wang, Q.; Gao, G. F.; Yuan, Z.; Yan, J. A Human Neutralizing Antibody Targets the Receptor-Binding Site of SARS-CoV-2. *Nature* **2020**, *584* (7819), 120−124.
(59) Heinicke, E.; Kumar, U.; Munoz, D. G. Quantitative Dot-Blot Assay for Proteins Using Enhanced Chemiluminescence. *J. Immunol. Methods* **1992**, *152* (2), 227−236.
(60) Steppert, P.; Burgstaller, D.; Klausberger, M.; Tover, A.; Berger, E.; Jungbauer, A. Quantification and Characterization of Virus-like Particles by Size-Exclusion Chromatography and Nanoparticle Tracking Analysis. *J. Chromatogr. A* **2017**, *1487*, 89−99.
(61) Šagi, D.; Kienz, P.; Denecke, J.; Marquardt, T.; Peter-Katalinić, J. Glycoproteomics OfN-Glycosylation by in-Gel Deglycosylation and Matrix-Assisted Laser Desorption/Ionisation-Time of Flight Mass Spectrometry Mapping: Application to Congenital Disorders of Glycosylation. *Proteomics* **2005**, *5* (10), 2689−2701.
(62) Herrera, N. G.; Morano, N. C.; Celikgil, A.; Georgiev, G. I.; Malonis, R. J.; Lee, J. H.; Tong, K.; Vergnolle, O.; Massimi, A. B.; Yen, L. Y.; Noble, A. J.; Kopylov, M.; Bonanno, J. B.; Garrett-Thomson, S. C.; Hayes, D. B.; Bortz, R. H.; Wirchnianski, A. S.; Florez, C.; Laudermilch, E.; Haslwanter, D.; Fels, J. M.; Dieterle, M. E.; Jangra, R. K.; Barnhill, J.; Mengotto, A.; Kimmel, D.; Daily, J. P.; Pirofski, L.; Chandran, K.; Brenowitz, M.; Garforth, S. J.; Eng, E. T.; Lai, J. R.; Almo, S. C. Characterization of the SARS-CoV-2 S Protein: Biophysical, Biochemical, Structural, and Antigenic Analysis. *ACS Omega* **2020**, in press. DOI: 10.1021/acsomega.0c03512.
(63) Bornholdt, Z. A.; Turner, H. L.; Murin, C. D.; Li, W.; Sok, D.; Souders, C. A.; Piper, A. E.; Goff, A.; Shamblin, J. D.; Wollen, S. E.; Sprague, T. R.; Fusco, M. L.; Pommert, K. B. J.; Cavacini, L. A.; Smith, H. L.; Klempner, M.; Reimann, K. A.; Krauland, E.; Gerngross, T. U.; Wittrup, K. D.; Saphire, E. O.; Burton, D. R.; Glass, P. J.; Ward, A. B.; Walker, L. M. Isolation of Potent Neutralizing Antibodies from a Survivor of the 2014 Ebola Virus Outbreak. *Science* **2016**, *351* (6277), 1078−1083.
(64) Vandepapelière, P.; Horsmans, Y.; Moris, P.; Van Mechelen, M.; Janssens, M.; Koutsoukos, M.; Van Belle, P.; Clement, F.; Hanon, E.; Wettendorff, M.; Garçon, N.; Leroux-Roels, G. Vaccine Adjuvant Systems Containing Monophosphoryl Lipid A and QS21 Induce Strong and Persistent Humoral and T Cell Responses against Hepatitis B Surface Antigen in Healthy Adult Volunteers. *Vaccine* **2008**, *26* (10), 1375−1386.
(65) Leroux-Roels, G.; Van Belle, P.; Vandepapeliere, P.; Horsmans, Y.; Janssens, M.; Carletti, I.; Garçon, N.; Wettendorff, M.; Van Mechelen, M. Vaccine Adjuvant Systems Containing Monophosphoryl Lipid A and QS-21 Induce Strong Humoral and Cellular Immune Responses against Hepatitis B Surface Antigen Which Persist for at Least 4 Years after Vaccination. *Vaccine* **2015**, *33* (8), 1084−1091.
(66) Marty-Roix, R.; Vladimer, G. I.; Pouliot, K.; Weng, D.; Buglione-Corbett, R.; West, K.; MacMicking, J. D.; Chee, J. D.; Wang, S.; Lu, S.; Lien, E. Identification of QS-21 as an Inflammasome-Activating Molecular Component of Saponin Adjuvants. *J. Biol. Chem.* **2016**, *291* (3), 1123−1136.
(67) Case, J. B.; Rothlauf, P. W.; Chen, R. E.; Liu, Z.; Zhao, H.; Kim, A. S.; Bloyet, L.; Zeng, Q.; Tahan, S.; Droit, L.; Ilagan, M. X. G.; Tartell, M. A.; Amarasinghe, G.; Henderson, J. P.; Miersch, S.; Ustav, M.; Sidhu, S.; Virgin, H. W.; Wang, D.; Ding, S.; Corti, D.; Theel, E. S.; Fremont, D. H.; Diamond, M. S.; Whelan, S. P. J. Neutralizing Antibody and Soluble ACE2 Inhibition of a Replication-Competent VSV-SARS-CoV-2 and a Clinical Isolate of SARS-CoV-2. *Cell Host Microbe* **2020**, *28*, 475.
(68) Mandolesi, M.; Sheward, D. J.; Hanke, L.; Ma, J.; Pushparaj, P.; Vidakovics, L. P.; Kim, C.; Loré, K.; Dopico, X. C.; Coquet, J. M.; McInerney, G.; Karlsson Hedestam, G. B.; Murrell, B. SARS-CoV-2 Protein Subunit Vaccination Elicits Potent Neutralizing Antibody Responses. *bioRxiv*, 2020. DOI: 10.1101/2020.07.31.228486.
(69) Chi, X.; Yan, R.; Zhang, J.; Zhang, G.; Zhang, Y.; Hao, M.; Zhang, Z.; Fan, P.; Dong, Y.; Yang, Y.; Chen, Z.; Guo, Y.; Zhang, J.; Li, Y.; Song, X.; Chen, Y.; Xia, L.; Fu, L.; Hou, L.; Xu, J.; Yu, C.; Li, J.; Zhou, Q.; Chen, W. A Neutralizing Human Antibody Binds to the N-Terminal Domain of the Spike Protein of SARS-CoV-2. *Science* **2020**, *369* (6504), 650−655.
(70) Lefeber, D. J.; Benaissa-Trouw, B.; Vliegenthart, J. F. G.; Kamerling, J. P.; Jansen, W. T. M.; Kraaijeveld, K.; Snippe, H. Th1-Directing Adjuvants Increase the Immunogenicity of Oligosaccharide-Protein Conjugate Vaccines Related to Streptococcus Pneumoniae Type 3. *Infect. Immun.* **2003**, *71*, 6915.
(71) Visciano, M. L.; Tagliamonte, M.; Tornesello, M. L.; Buonaguro, F. M.; Buonaguro, L. Effects of Adjuvants on IgG Subclasses Elicited by Virus-like Particles. *J. Transl. Med.* **2012**, *10* (1), 4.
(72) Bos, R.; Rutten, L.; van der Lubbe, J. E. M.; Bakkers, M. J. G.; Hardenberg, G.; Wegmann, F.; Zuijdgeest, D.; de Wilde, A. H.; Koornneef, A.; Verwilligen, A.; van Manen, D.; Kwaks, T.; Vogels, R.; Dalebout, T. J.; Myeni, S. K.; Kikkert, M.; Snijder, E. J.; Li, Z.; Barouch, D. H.; Vellinga, J.; Langedijk, J. P. M.; Zahn, R. C.; Custers, J.; Schuitemaker, H. Ad26 Vector-Based COVID-19 Vaccine Encoding a Prefusion-Stabilized SARS-CoV-2 Spike Immunogen Induces Potent Humoral and Cellular Immune Responses. *npj Vaccines* **2020**, in press. DOI: 10.1038/s41541-020-00243-x.
(73) Lederer, K.; Castaño, D.; Atria, D. G.; Oguin, T. H.; Wang, S.; Manzoni, T. B.; Muramatsu, H.; Hogan, M. J.; Amanat, F.; Cherubin, P.; Lundgreen, K. A.; Tam, Y. K.; Fan, S. H. Y.; Eisenlohr, L. C.; Maillard, I.; Weissman, D.; Bates, P.; Krammer, F.; Sempowski, G. D.; Pardi, N.; Locci, M. SARS-CoV-2 MRNA Vaccines Foster Potent Antigen-Specific Germinal Center Responses Associated with Neutralizing Antibody Generation. *Immunity* **2020**, *53*, 1281.
(74) Dong, Y.; Dai, T.; Wei, Y.; Zhang, L.; Zheng, M.; Zhou, F. A Systematic Review of SARS-CoV-2 Vaccine Candidates. *Signal Transduct. Target. Ther.* **2020**, *5* (1), 237.
(75) Iwata-Yoshikawa, N.; Uda, A.; Suzuki, T.; Tsunetsugu-Yokota, Y.; Sato, Y.; Morikawa, S.; Tashiro, M.; Sata, T.; Hasegawa, H.; Nagata, N. Effects of Toll-Like Receptor Stimulation on Eosinophilic

Infiltration in Lungs of BALB/c Mice Immunized with UV-Inactivated Severe Acute Respiratory Syndrome-Related Coronavirus Vaccine. *J. Virol.* **2014**, *88* (15), 8597−8614.
(76) Honda-Okubo, Y.; Barnard, D.; Ong, C. H.; Peng, B.-H.; Tseng, C.-T. K.; Petrovsky, N. Severe Acute Respiratory Syndrome-Associated Coronavirus Vaccines Formulated with Delta Inulin Adjuvants Provide Enhanced Protection While Ameliorating Lung Eosinophilic Immunopathology. *J. Virol.* **2015**, *89* (6), 2995−3007.
(77) Tseng, C.-T.; Sbrana, E.; Iwata-Yoshikawa, N.; Newman, P. C.; Garron, T.; Atmar, R. L.; Peters, C. J.; Couch, R. B. Immunization with SARS Coronavirus Vaccines Leads to Pulmonary Immunopathology on Challenge with the SARS Virus. *PLoS One* **2012**, *7* (4), No. e35421.
(78) Vartak, A.; Sucheck, S. Recent Advances in Subunit Vaccine Carriers. *Vaccines* **2016**, *4* (2), 12.
(79) Tai, W.; He, L.; Zhang, X.; Pu, J.; Voronin, D.; Jiang, S.; Zhou, Y.; Du, L. Characterization of the Receptor-Binding Domain (RBD) of 2019 Novel Coronavirus: Implication for Development of RBD Protein as a Viral Attachment Inhibitor and Vaccine. *Cell. Mol. Immunol.* **2020**, *17* (6), 613−620.
(80) Tai, W.; Zhang, X.; Drelich, A.; Shi, J.; Hsu, J. C.; Luchsinger, L.; Hillyer, C. D.; Tseng, C.-T. K.; Jiang, S.; Du, L. A Novel Receptor-Binding Domain (RBD)-Based MRNA Vaccine against SARS-CoV-2. *Cell Res.* **2020**, *30*, 932.
(81) Misasi, J.; Gilman, M. S. A.; Kanekiyo, M.; Gui, M.; Cagigi, A.; Mulangu, S.; Corti, D.; Ledgerwood, J. E.; Lanzavecchia, A.; Cunningham, J.; Muyembe-Tamfun, J. J.; Baxa, U.; Graham, B. S.; Xiang, Y.; Sullivan, N. J.; McLellan, J. S. Structural and Molecular Basis for Ebola Virus Neutralization by Protective Human Antibodies. *Science* **2016**, *351* (6279), 1343−1346.
(82) Scheres, S. H. W. RELION: Implementation of a Bayesian Approach to Cryo-EM Structure Determination. *J. Struct. Biol.* **2012**, *180* (3), 519−530.
(83) Zheng, S. Q.; Palovcak, E.; Armache, J.-P.; Verba, K. A.; Cheng, Y.; Agard, D. A. MotionCor2: Anisotropic Correction of Beam-Induced Motion for Improved Cryo-Electron Microscopy. *Nat. Methods* **2017**, *14* (4), 331−332.
(84) Rohou, A.; Grigorieff, N. CTFFIND4: Fast and Accurate Defocus Estimation from Electron Micrographs. *J. Struct. Biol.* **2015**, *192* (2), 216−221.
(85) Tang, G.; Peng, L.; Baldwin, P. R.; Mann, D. S.; Jiang, W.; Rees, I.; Ludtke, S. J. EMAN2: An Extensible Image Processing Suite for Electron Microscopy. *J. Struct. Biol.* **2007**, *157* (1), 38−46.
(86) Punjani, A.; Rubinstein, J. L.; Fleet, D. J.; Brubaker, M. A. CryoSPARC: Algorithms for Rapid Unsupervised Cryo-EM Structure Determination. *Nat. Methods* **2017**, *14* (3), 290−296.
(87) Pettersen, E. F.; Goddard, T. D.; Huang, C. C.; Couch, G. S.; Greenblatt, D. M.; Meng, E. C.; Ferrin, T. E. UCSF Chimera?A Visualization System for Exploratory Research and Analysis. *J. Comput. Chem.* **2004**, *25* (13), 1605−1612.

https://dx.doi.org/10.1021/acscentsci.0c01405
ACS Cent. Sci. 2021, 7, 183−199

Supplemental Information

Table of contents:

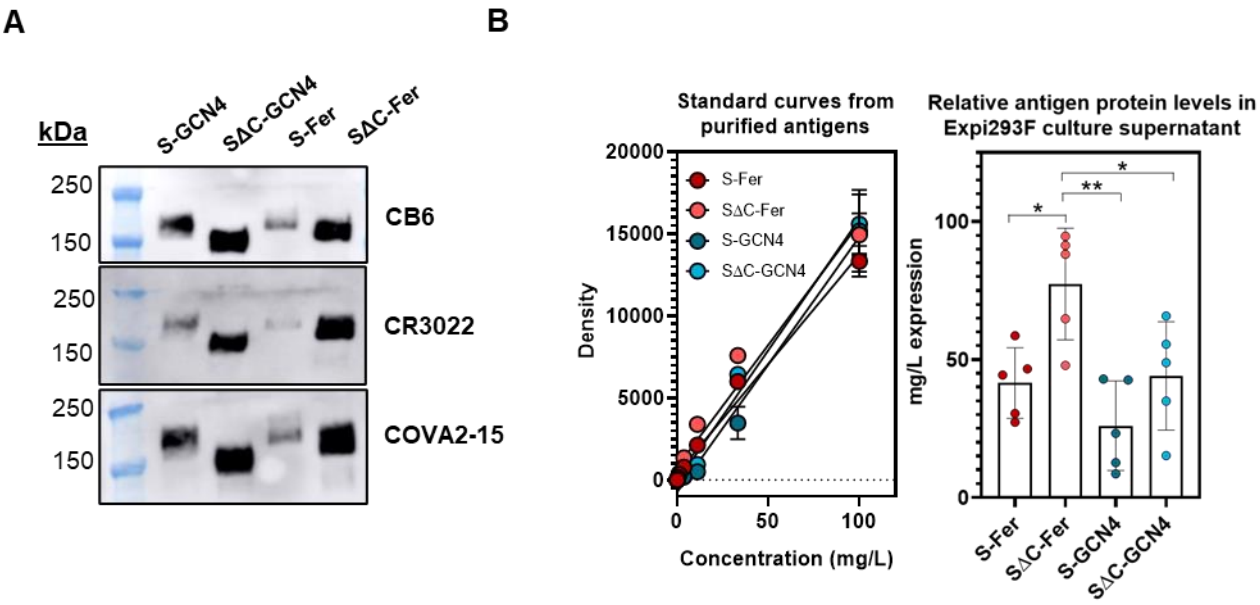

Figure S1. Spike ferritin nanoparticles are expressed at levels similar to those of spike GCN4 trimers. (A) Western blot analysis of Expi293F culture supernatant indicates that expression levels are similar among the spike antigen constructs. Supernatants were blotted with CB6 (top), CR3022 (middle), or COVA2-15 (bottom) SARS-CoV-2 mAbs and read out using an anti-human HRP secondary. (B) Dot blot analysis was performed to estimate protein levels of spike antigens in culture supernatants. Purified antigens were used to generate standard curves using a 3-fold dilution series starting at 0.1 mg/mL (*59*). Dots were quantified using CR3022 primary mAb followed by anti-human HRP secondary. Standard curves were then used to calculate the amount of protein in harvested culture supernatants from 5 replicate protein expressions. The height of the bar is the mean protein concentration from 5 individual protein expression replicates (points) from culture supernatant; error bars represent the standard deviation. Statistical comparison of expression levels was performed using ordinary one-way ANOVA followed by Tukey's multiple comparisons test. All *p* values are represented as followed: * = $p \leq 0.05$, ** = $p \leq 0.01$, *** = $p \leq 0.001$, **** = $p \leq 0.0001$

A

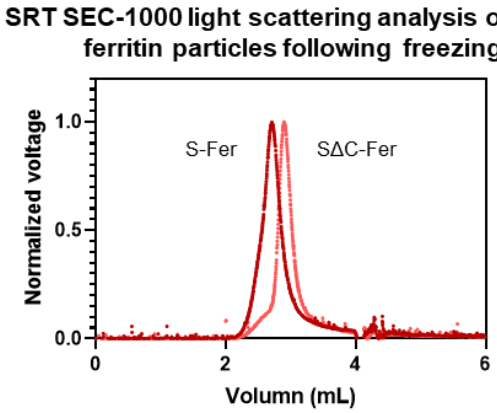

B

Spike ferritin construct	SEC-MALS determined molecular weight (Da)	Predicted molecular weight based on amino acid sequence (Da)
S-Fer	$4.2 \pm 0.17 \times 10^6$	3.7×10^6
SΔC-Fer	$3.1 \pm 0.24 \times 10^6$	3.5×10^6

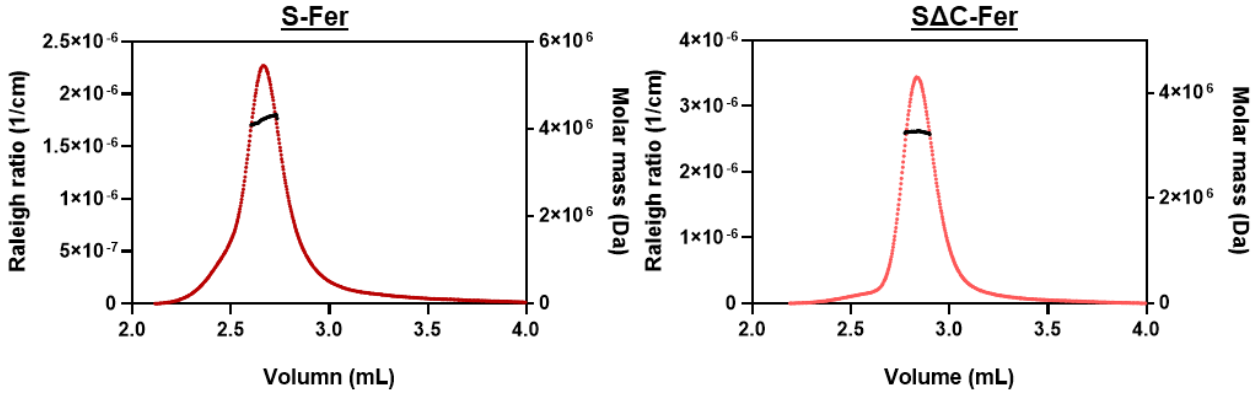

C

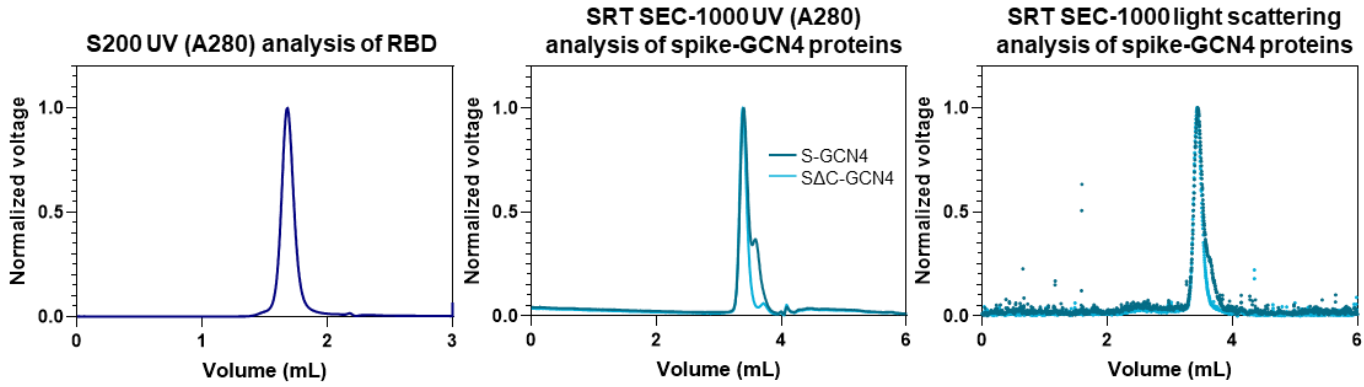

Figure S2. Size-exclusion chromatography multi-angle light scattering molecular weight determination of spike ferritin nanoparticles and analysis of other antigens. (A) Light scattering analysis of the S-Fer and SΔC-Fer particles on the SRT SEC-1000 analytical column indicate that particles do not aggregate following a freeze-thaw cycle. Glycerol (10%) was added to particle samples prior to snap-freezing. (B) Molecular weight calculation for S-Fer and SΔC-Fer determined by SEC-MALS was performed with ASTRA software using light scattering and refractive index signals for the particles. The average calculated molecular weight obtained from two independent protein preparations for each particle (S-Fer and SΔC-Fer) is shown. The expected molecular weight was determined by the amino acid sequence for the individual S-Fer and SΔC-Fer protomers and multiplied by 24 to account for the number of protomers in a particle. The expected mass does not account for glycosylation; each protomer contains ~20 predicted N-linked glycans which could add up to 1 MDa to the mass of the particle (*61*). Discrepancies in calculated and expected molecular weights could in part be due to incomplete glycosylation. The plots show a representative curve from each analysis. The colored traces correspond to the left y-axis which shows the Rayleigh ratio, a measure of light scattering. The black line on each peak is the calculated molecular weight, plotted on the right y-axis, as a function of particle elution. This demonstrates that the molecular weight calculation is not subject to variations resulting from artifacts in the eluted peak. (C) SEC-MALS traces for the RBD, S-GCN4, and SΔC-GCN4 demonstrating that samples are pure and do not form aggregates. Only UV A280 is shown for the RBD because it is too small for light scattering to be detected with the miniDAWN detector.

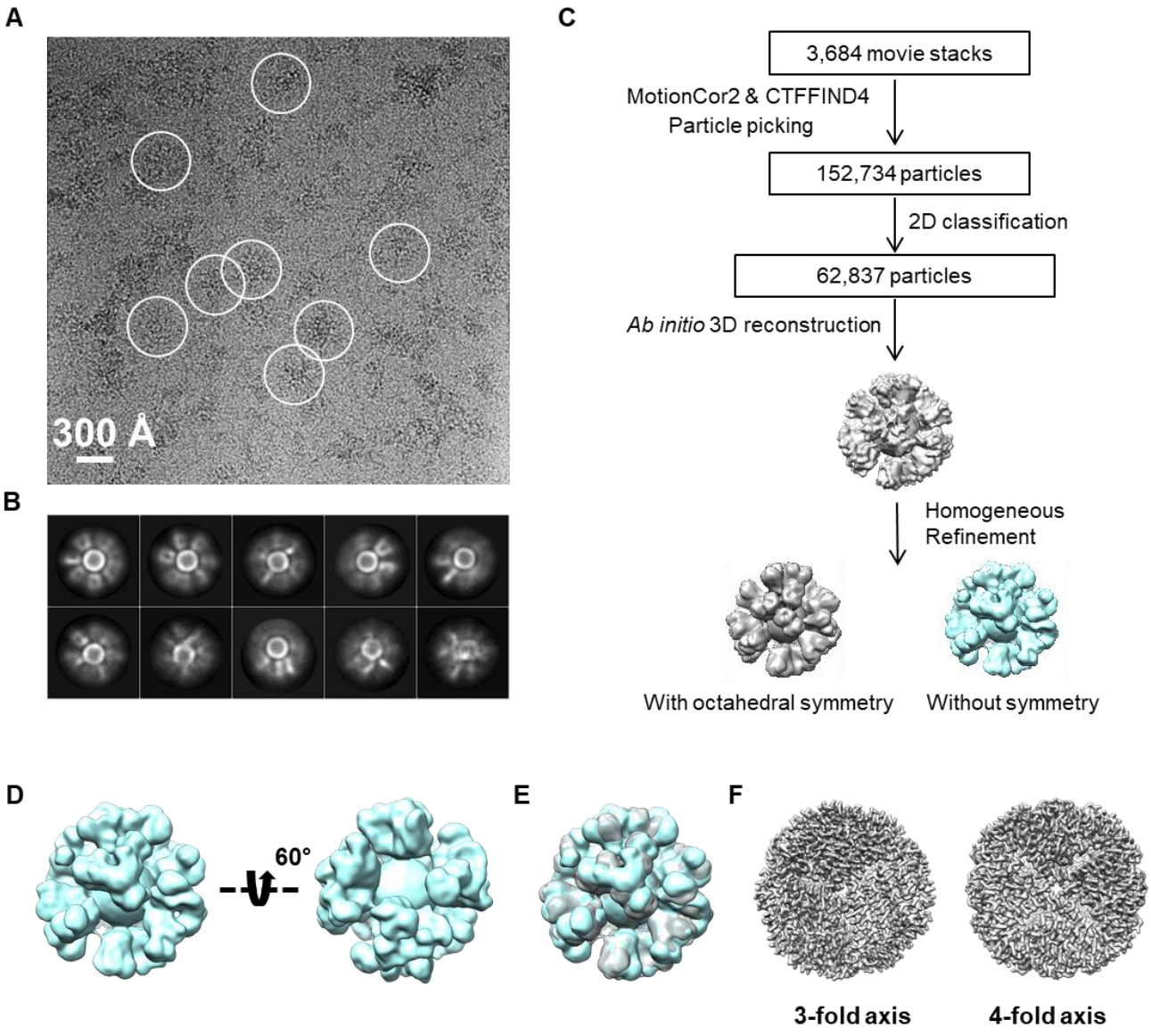

Figure S3. Cryo-EM of S-Fer and SΔC-Fer nanoparticles confirms the presence of spike proteins displayed on the surface of ferritin. (A) Representative motion-corrected cryo-EM micrograph of S-Fer with particles circled in white. (B) Reference-free 2D class averages of S-Fer nanoparticles from analysis of S-Fer indicating the presence of spike on the surface of the particles. (C) Workflow of cryo-EM data processing of SΔC-Fer. (D) Reconstructed cryo-EM map of the SΔC-Fer without symmetry applied (two views). (E) Superimposition (cyan and gray) of the two 3D reconstructions of SΔC-Fer with and without octahedral symmetry demonstrate that the two maps have high similarity, with a cross-correlation coefficient of 0.99. (F) Single-particle analysis focused on the ferritin core from the SΔC-Fer dataset. The 3.7-Å resolution reconstructed cryo-EM map is shown in two different views. Left, 3-fold view; Right, 4-fold view.

A

Antigen	Monomer (nM)	Trimer / nanoparticle (nM)	CB6 IgG k_{on} (M^{-1} s^{-1})	COVA2-15 IgG k_{on} (M^{-1} s^{-1})	CR3022 IgG k_{on} (M^{-1} s^{-1})
S-Fer	100	4.2	$5.9 \pm 0.34 \times 10^5$	$5.4 \pm 1.1 \times 10^5$	$4.9 \pm 4.0 \times 10^5$
SΔC-Fer	100	4.2	$9.9 \pm 3.8 \times 10^5$	$1.1 \pm 0.32 \times 10^6$	$7.3 \pm 5.3 \times 10^5$
S-GCN4	100	33.3	$4.1 \pm 1.1 \times 10^5$	$4.3 \pm 0.80 \times 10^5$	$2.3 \pm 0.42 \times 10^5$
SΔC-GCN4	100	33.3	$4.1 \pm 0.16 \times 10^5$	$4.9 \pm 0.081 \times 10^5$	$2.3 \pm 0.073 \times 10^5$
RBD	100	--	$1.9 \pm 0.16 \times 10^5$	$4.9 \pm 0.66 \times 10^5$	$3.2 \pm 0.70 \times 10^5$

B

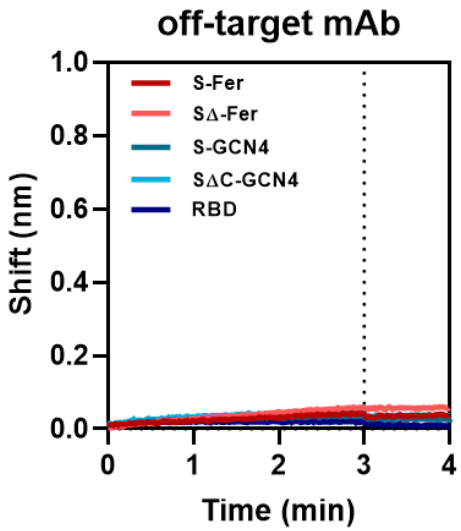

Figure S4. SARS-CoV-2 antigens bind to conformation specific mAbs with similar k_{on} values and do not show non-specific binding. (A) Binding curves shown in Figure 3D were fit with a non-linear association/dissociation equation to obtain kinetic binding parameters. Several binding interactions did not have quantifiable off-rates and thus k_{on} values are presented as a comparative measure of each mAb binding to each antigen in the panel. (B) BLI shows that antigens do not bind non-specifically to an off-target Ebola-specific monoclonal antibody, ADI-15731, confirming the specificity of observed binding shown in Figure 3D.

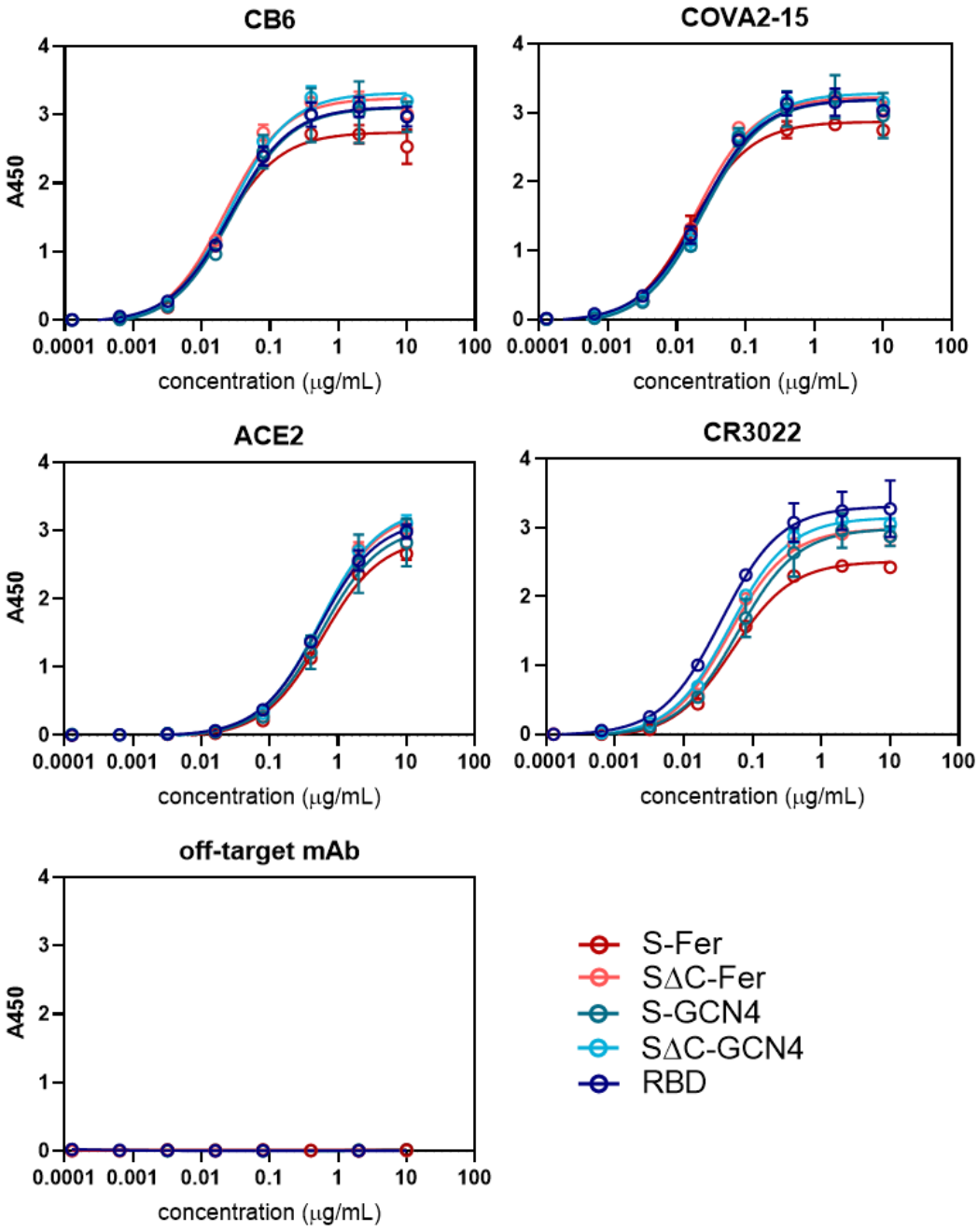

Figure S5. ELISA confirms that the ACE2 binding site and mAb epitopes are displayed on spike ferritin similarly to their display in the RBD and spike trimers. For ELISA, antigens were hydrophobically plated at 2 μg/mL and binding of human ACE2 and a set of SARS-CoV-2 antibodies was assessed. ELISA reveals that ACE2 and mAbs bind all antigens in a similar manner. Dilution series of hACE2 and mAbs starting at 10 μg/mL were bound to coated antigens. Binding was quantified using an anti-human-Fc HRP secondary. Each binding curve represents the average binding from 4 replicates and error bars are the standard deviation.

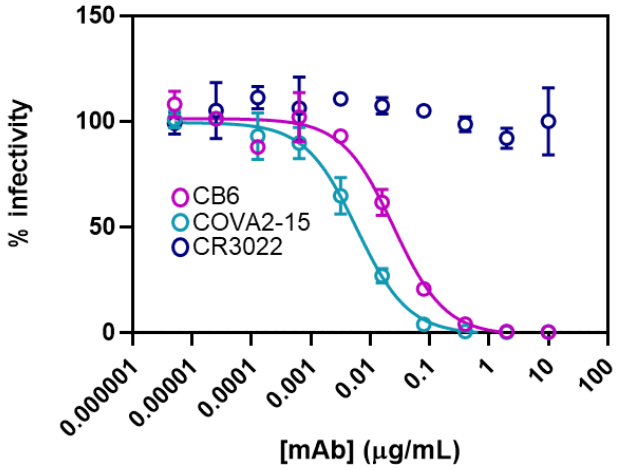

Neutralizing mAb	Determined IC_{50} value (µg/mL)	Literature IC_{50} value (µg/mL)
CB6	0.02 ± 0.009	0.036
COVA2-15	0.004 ± 0.002	0.008

Figure S6. Validation of a SARS-CoV-2 neutralization assay using a spike-pseudotyped lentivirus. The spike pseudotyped lentivirus assay was validated using two published SARS-CoV-2 neutralizing mAbs (CB6 (*58*) and COVA2-15 (*5*)) and one SARS-CoV-2 reactive mAb known to be non-neutralizing (CR3022) (*55-57*). CB6 and COVA2-15 dilution curves were fit with a three-parameter non-linear regression to obtain IC_{50} values (Methods). Neutralization assays were performed in technical duplicate or triplicate in 4 independent experiments and one representative curve is shown. Mean IC_{50} values from replicates are shown in the table with standard deviation.

	S-Fer	SΔC-Fer	S-GCN4	SΔC-GCN4	RBD	CCP
Day 21 (Prime only)						
RBD IgG ELISA titer (EC_{50})	$3.2 \pm 1.6 \times 10^3$	$6.0 \pm 4.3 \times 10^3$	$2.0 \pm 1.5 \times 10^3$	$1.3 \pm 1.7 \times 10^3$	$3.0 \pm 6.0 \times 10^3$	---
Spike IgG ELISA titer (EC_{50})	$6.1 \pm 3.3 \times 10^3$	$8.7 \pm 6.5 \times 10^3$	$5.2 \pm 2.7 \times 10^3$	$2.2 \pm 2.6 \times 10^3$	$2.4 \pm 1.3 \times 10^2$	---
% ACE2 blocking (1:50)	33 ± 14	45 ± 18	17 ± 7.6	13 ± 15	12 ± 6.5	---
% ACE2 blocking (1:500)	0.62 ± 2.3	2.8 ± 1.8	1.4 ± 1.6	4.4 ± 3.0	1.4 ± 2.5	---
Spike-pseudotyped lentivirus neutralizing titer (IC_{50})	$1.1 \pm 1.2 \times 10^3$	$1.6 \pm 1.2 \times 10^3$	$1.9 \pm 1.2 \times 10^2$	$1.2 \pm 0.69 \times 10^2$	1.0×10^2 (LOQ)	$6.2 \pm 6.3 \times 10^2$
Day 28 (Prime + Boost)						
RBD IgG ELISA titer (EC_{50})	$2.9 \pm 1.3 \times 10^4$	$8.2 \pm 4.8 \times 10^4$	$7.4 \pm 4.9 \times 10^4$	$5.2 \pm 3.9 \times 10^4$	$9.2 \pm 6.9 \times 10^4$	---
Spike IgG ELISA titer (EC_{50})	$6.6 \pm 2.5 \times 10^4$	$1.2 \pm 0.66 \times 10^5$	$1.9 \pm 1.2 \times 10^5$	$8.8 \pm 5.9 \times 10^4$	$5.4 \pm 3.6 \times 10^4$	---
% ACE2 blocking (1:50)	94 ± 15	99 ± 0.67	96 ± 9.3	93 ± 9.4	93 ± 14	---
% ACE2 blocking (1:500)	22 ± 8.1	50 ± 23	46 ± 21	44 ± 24	61 ± 26	---
Spike-pseudotyped lentivirus neutralizing titer (IC_{50})	$1.2 \pm 0.53 \times 10^4$	$3.4 \pm 2.5 \times 10^4$	$8.8 \pm 7.2 \times 10^3$	$9.4 \pm 13.4 \times 10^3$	$1.5 \pm 1.7 \times 10^4$	$6.2 \pm 6.3 \times 10^2$

Table S1. Mean ELISA binding titers, % ACE2 blocking, and spike-pseudotyped lentivirus neutralization titers from antigen groups at day 21 and day 28 post immunization. Each value represents the mean EC_{50} titer (ELISA binding), the mean % ACE2 blocking, or the mean IC_{50} titer (spike-pseudotyped lentivirus neutralization) for each antigen group at day 21 and day 28. Error represents the standard deviation.

Day 21 RBD ELISA titers

Dunn's multiple comparisons test	Mean rank diff.	Significant?	Summary	Adjusted *P* Value
RBD vs. SΔC-GCN4	3.200	No	*ns*	>0.9999
RBD vs. S-GCN4	-3.300	No	*ns*	>0.9999
RBD vs. SΔC-Fer	-20.70	Yes	*	0.0150
RBD vs. S-Fer	-10.70	No	*ns*	>0.9999
SΔC-GCN4 vs. S-GCN4	-6.500	No	*ns*	>0.9999
SΔC-GCN4 vs. SΔC-Fer	-23.90	Yes	**	0.0025
SΔC-GCN4 vs. S-Fer	-13.90	No	*ns*	0.3299
S-GCN4 vs. SΔC-Fer	-17.40	No	*ns*	0.0761
S-GCN4 vs. S-Fer	-7.400	No	*ns*	>0.9999
SΔC-Fer vs. S-Fer	10.00	No	*ns*	>0.9999

Day 21 Spike ELISA titers

Dunn's multiple comparisons test	Mean rank diff.	Significant?	Summary	Adjusted *P* Value
RBD vs. SΔC-GCN4	-13.50	No	*ns*	0.3837
RBD vs. S-GCN4	-23.20	Yes	**	0.0037
RBD vs. SΔC-Fer	-31.20	Yes	****	<0.0001
RBD vs. S-Fer	-26.10	Yes	***	0.0006
SΔC-GCN4 vs. S-GCN4	-9.700	No	*ns*	>0.9999
SΔC-GCN4 vs. SΔC-Fer	-17.70	No	*ns*	0.0663
SΔC-GCN4 vs. S-Fer	-12.60	No	*ns*	0.5326
S-GCN4 vs. SΔC-Fer	-8.000	No	*ns*	>0.9999
S-GCN4 vs. S-Fer	-2.900	No	*ns*	>0.9999
SΔC-Fer vs. S-Fer	5.100	No	*ns*	>0.9999

Day 28 RBD ELISA titers

Dunn's multiple comparisons test	Mean rank diff.	Significant?	Summary	Adjusted *P* Value
RBD vs. SΔC-GCN4	11.10	No	*ns*	0.8863
RBD vs. S-GCN4	3.200	No	*ns*	>0.9999
RBD vs. SΔC-Fer	0.8000	No	*ns*	>0.9999
RBD vs. S-Fer	20.40	Yes	*	0.0175
SΔC-GCN4 vs. S-GCN4	-7.900	No	*ns*	>0.9999
SΔC-GCN4 vs. SΔC-Fer	-10.30	No	*ns*	>0.9999
SΔC-GCN4 vs. S-Fer	9.300	No	*ns*	>0.9999
S-GCN4 vs. SΔC-Fer	-2.400	No	*ns*	>0.9999
S-GCN4 vs. S-Fer	17.20	No	*ns*	0.0833
SΔC-Fer vs. S-Fer	19.60	Yes	*	0.0264

Day 28 Spike ELISA titers

Dunn's multiple comparisons test	Mean rank diff.	Significant?	Summary	Adjusted *P* Value
RBD vs. SΔC-GCN4	-8.300	No	*ns*	>0.9999
RBD vs. S-GCN4	-22.70	Yes	**	0.0050
RBD vs. SΔC-Fer	-16.60	No	*ns*	0.1089
RBD vs. S-Fer	-4.400	No	*ns*	>0.9999
SΔC-GCN4 vs. S-GCN4	-14.40	No	*ns*	0.2718
SΔC-GCN4 vs. SΔC-Fer	-8.300	No	*ns*	>0.9999
SΔC-GCN4 vs. S-Fer	3.900	No	*ns*	>0.9999
S-GCN4 vs. SΔC-Fer	6.100	No	*ns*	>0.9999
S-GCN4 vs. S-Fer	18.30	Yes	*	0.0500
SΔC-Fer vs. S-Fer	12.20	No	*ns*	0.6129

Table S2. Statistical analysis of spike and RBD ELISA titers from day 21 and day 28 immunization timepoints. Calculated EC_{50} values for each animal for RBD and spike at each time point were compiled by group and assessed using a Kruskal-Wallis ANOVA followed by Dunn's multiple comparisons test. Pairwise comparisons are shown.

Day 21 pseudovirus neutralization titers

Dunn's multiple comparisons test	Mean rank diff.	Significant?	Summary	Adjusted P Value
RBD vs. SΔC-GCN4	-1.750	No	ns	>0.9999
RBD vs. S-GCN4	-7.300	No	ns	>0.9999
RBD vs. SΔC-Fer	-26.80	Yes	****	<0.0001
RBD vs. S-Fer	-19.15	Yes	*	0.0122
SΔC-GCN4 vs. S-GCN4	-5.550	No	ns	>0.9999
SΔC-GCN4 vs. SΔC-Fer	-25.05	Yes	***	0.0002
SΔC-GCN4 vs. S-Fer	-17.40	Yes	*	0.0329
S-GCN4 vs. SΔC-Fer	-19.50	Yes	**	0.0099
S-GCN4 vs. S-Fer	-11.85	No	ns	0.4531
SΔC-Fer vs. S-Fer	7.650	No	ns	>0.9999

Day 28 pseudovirus neutralization titers

Dunn's multiple comparisons test	Mean rank diff.	Significant?	Summary	Adjusted P Value
RBD vs. SΔC-GCN4	5.900	No	ns	>0.9999
RBD vs. S-GCN4	2.800	No	ns	>0.9999
RBD vs. SΔC-Fer	-15.70	No	ns	0.1603
RBD vs. S-Fer	-4.000	No	ns	>0.9999
SΔC-GCN4 vs. S-GCN4	-3.100	No	ns	>0.9999
SΔC-GCN4 vs. SΔC-Fer	-21.60	Yes	**	0.0092
SΔC-GCN4 vs. S-Fer	-9.900	No	ns	>0.9999
S-GCN4 vs. SΔC-Fer	-18.50	Yes	*	0.0454
S-GCN4 vs. S-Fer	-6.800	No	ns	>0.9999
SΔC-Fer vs. S-Fer	11.70	No	ns	0.7270

Table S3. Statistical analysis of spike and RBD neuralization titers from day 21 and day 28 immunization timepoints. Calculated neutralization IC_{50} values for each animal at each time point were compiled by group and assessed using a Kruskal-Wallis ANOVA followed by Dunn's multiple comparisons test. Pairwise comparisons are shown.

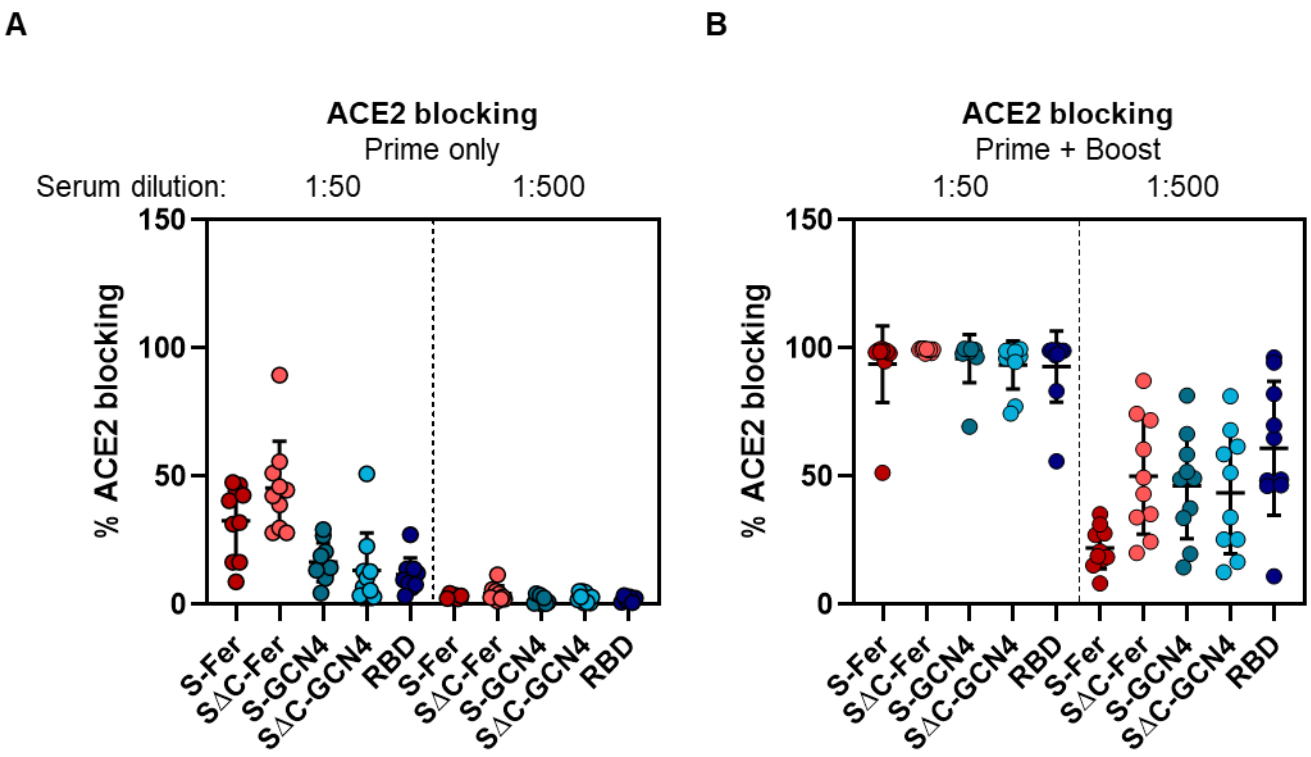

Figure S7. **Sera from mice immunized with SARS-CoV-2 block ACE2 binding to RBD, as indicated by ELISA.** (A) ACE2 blocking activity of sera from mice immunized with a single dose of antigen was determined using an RBD-based ELISA in which RBD-coated plates were incubated with serum dilutions and then ACE2 binding was assayed. ACE2 blocking at a 1:50 and 1:500 serum dilution is shown for each group, and indicates that following a single dose, minimal ACE2 blocking activity is seen in the serum evenat a high concentration. No groups show detectable ACE2 blocking activity in the serum diluted at 1:500. Each point represents the average % ACE2 blocking for a single animal assayed in duplicate; each bar represents the mean % ACE2 blocking from the group (*n* = 10 mice per group); error bars represent standard deviation. (B) ACE2 blocking activity was assessed after two doses of antigen and indicates a notable increase in serum antibodies capable of blocking ACE2 binding to RBD. Nearly all ACE2 binding was blocked with a 1:50 serum dilution from all groups, and all groups had detectable blocking at 1:500. Groups and error are as defined in (A).

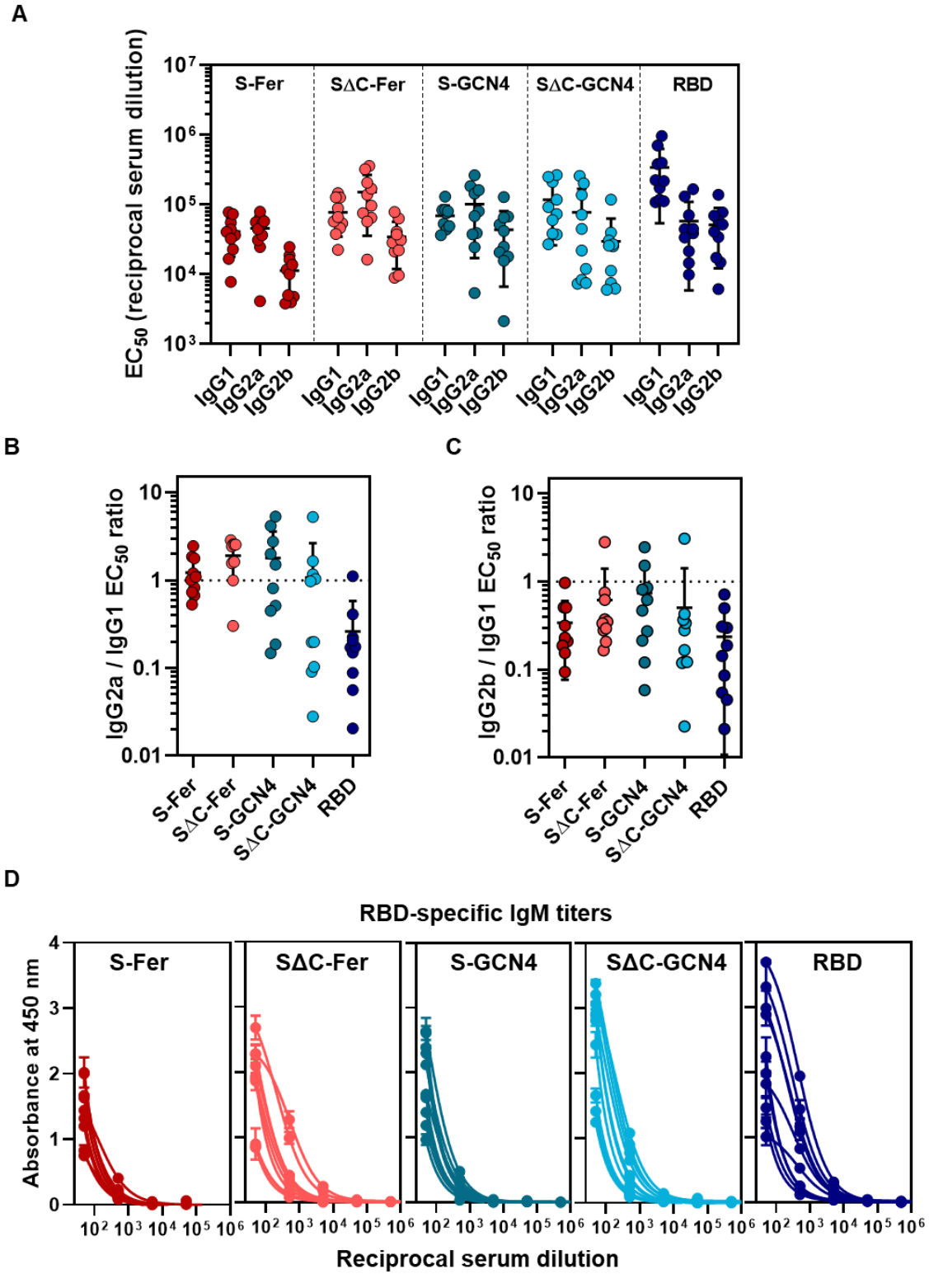
A
EC50 (reciprocal serum dilution)
S-Fer
SΔC-Fer
S-GCN4
SΔC-GCN4
RBD
IgG1
IgG2a
IgG2b
B
IgG2a / IgG1 EC50 ratio
C
IgG2b / IgG1 EC50 ratio
D
RBD-specific IgM titers
Absorbance at 450 nm
Reciprocal serum dilution

Figure S8. Immunization with SARS-CoV-2 antigens adjuvanted with Quil-A/MPLA leads to robust RBD-specific IgG1 and IgG2 isotype responses and minimal levels of IgM following two doses. (A) ELISA binding titers quantifying RBD-specific IgG1, IgG2a, and IgG2b subclass responses following two doses of antigen demonstrate broad IgG subclass elicitation with varied ratios among different antigen groups. Each point represents the EC_{50} titer from a single animal; each bar represents the mean EC_{50} titer from the group (*n* = 10 mice per group); error bars represent standard deviation. (B) Ratios of RBD-specific IgG2a/IgG1 following two doses of antigen for each group. SΔC-Fer and S-GCN4 groups exhibit higher IgG2a responses as compare to IgG1, whereas S-Fer and SΔC-GCN4 groups exhibit roughly balanced levels and the RBD group exhibits substantially greater IgG1 response. Each point represents the EC_{50} ratio from a single animal; each bar represents the mean EC_{50} ratio from the group (*n* = 10 mice per group); error bars represent standard deviation. (C) Ratios of RBD-specific IgG2b/IgG1 following two doses of antigen for each group. All groups exhibit mean IgG2b/IgG1 ratios less than 1, indicating a lower IgG2b response as compared to IgG1. Groups and error are as defined in (B). (D) RBD-specific IgM titers following two doses of antigen indicates lower levels of IgM as compared to IgG titers. Each curve represents an experimental replicate from each animal (*n* = 10 mice per group); error bars represent standard deviation for each point.

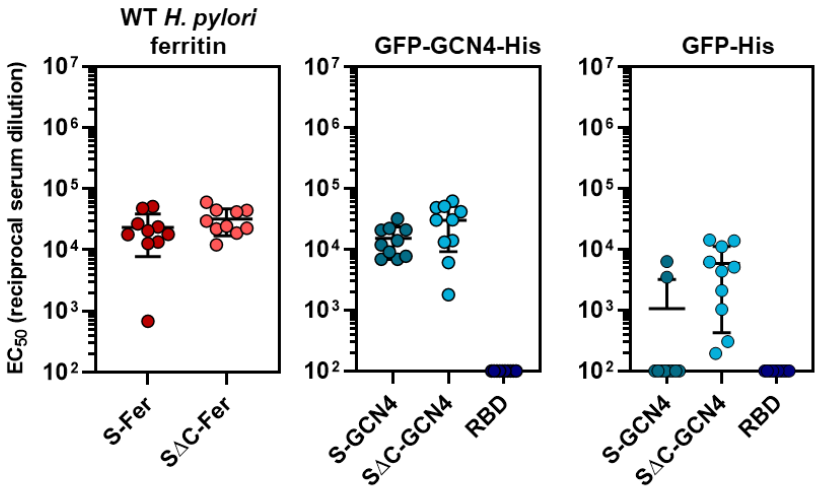

	S-Fer	SΔC-Fer	S-GCN4	SΔC-GCN4	RBD
WT *H. pylori* ferritin ELISA titers (EC_{50})	2.3 ± 1.6 x 10^4	3.2 ± 1.5 x 10^4	---	---	---
GFP-GCN4-His ELISA titers (EC_{50})	---	---	1.5 ± 0.84 x 10^4	3.0 ± 2.1 x 10^4	1.0 x 10^2 (LOQ)
GFP-His ELISA titers (EC_{50})	---	---	1.1 ± 2.1 x 10^3	5.9 ± 5.4 x 10^3	1.0 x 10^2 (LOQ)

Figure S9. Off-target antibody responses to either *H. pylori* ferritin or GCN4-trimerization domain are similar between ferritin and trimer immunization groups. ELISA binding titers against non-SARS-CoV-2 antigen domains following two doses of antigen reveal off-target responses that are similar or less than antigen-specific RBD and spike titers (see Figure 4D and Table S1). Each point represents the EC_{50} ratio from a single animal; each bar represents the mean EC_{50} ratio from the group (n = 10 mice per group); error bars represent standard deviation. Points with signal less than EC_{50} 1:100 dilution are placed at the limit of quantitation for the assay. Values shown in table correspond to mean titers for each group and error represents standard deviation.

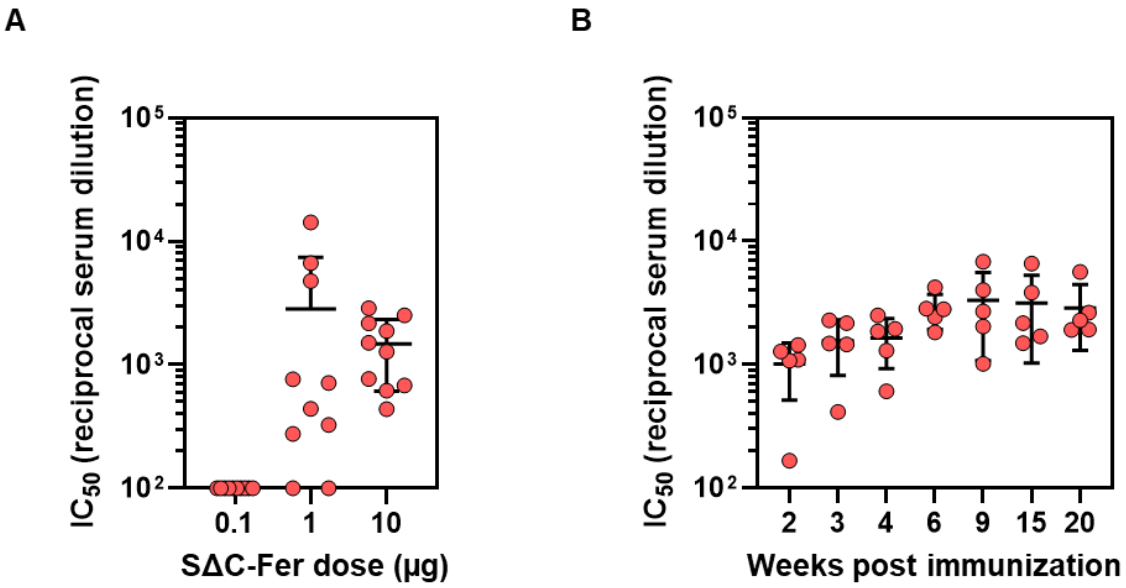

Figure S10. Immunization with SΔC-Fer leads to a dose-dependent neutralizing antibody response and elicits neutralizing antibody levels that are stable up to 20 weeks post immunization. (A) Neutralizing antibody responses against SΔC-Fer show dose-dependent trends. Mice (*n* = 10 per dose) were immunized with a single dose of either 0.1 μg, 1 μg, or 10 μg SΔC-Fer particles adjuvanted with 10 μg Quil-A / 10 μg MPLA via subcutaneous injection. Serum was collected at day 28 post immunization and analyzed for spike-pseudotyped lentivirus neutralization activity. Each point represents the IC_{50} titer from a single animal; each bar represents the mean IC_{50} titer from each group; error bars represent the standard deviation. Samples with neutralizing activity that was undetectable at 1:50 dilution or with an IC_{50} less than 1:100 dilution are placed at the limit of quantitation. (B) Neutralizing antibody responses increase between 2- and 6-weeks post immunization with 20 μg SΔC-Fer and remain stable to 20-weeks post immunization. Mice (*n* = 5) were immunized with a single dose of 20 μg SΔC-Fer particles adjuvanted with 10 μg Quil-A / 10 μg MPLA via subcutaneous injection. Serum was assessed at timepoints between 2- and 20-weeks post immunization for neutralization of spike-pseudotyped lentivirus. Groups and error are as described in (A).